Anoxia decreases the magnitude of the carbon, nitrogen, and phosphorus sink in freshwaters

Cayelan C. Carey[1]*, Paul C. Hanson[2], R. Quinn Thomas[1,3], Alexandra B. Gerling[1], Alexandria G. Hounshell[1], Abigail S. L. Lewis[1], Mary E. Lofton[1], Ryan P. McClure[1], Heather L. Wander[1], Whitney M. Woelmer[1], B. R. Niederlehner[1], Madeline E. Schreiber[4]

[1]Department of Biological Sciences, Virginia Tech, Blacksburg, Virginia, USA 24061.

[2]Center for Limnology, University of Wisconsin-Madison, Madison, Wisconsin, USA 53706.

[3]Department of Forest Resources and Environmental Conservation, Virginia Tech, Blacksburg, Virginia, USA 24061.

[4]Department of Geosciences, Virginia Tech, Blacksburg, Virginia, USA 24061.

*Corresponding author. Email: cayelan@vt.edu; Phone: +1-540-231-8938

Running head: Anoxia disrupts freshwater C, N, and P cycles

Author contributions: Conceptualization: CCC, PCH, MES; Data curation: CCC, ABG, AGH, ASL, MEL, RPM, HLW, WMW, BRN; Formal analysis: CCC, PCH, RQT; Investigation: CCC, ABG, AGH, ASL, MEL, RPM, HLW, WMW, BRN, MES; Methodology: CCC, PCH, RQT; Project administration: CCC; Software: RQT; Visualization: CCC, ASL, RPM, WMW, AGH, HLW; Supervision: CCC, MES; Writing-original draft: CCC, MEL, BRN, AGH; Writing-review & editing: CCC, PCH, RQT, ABG, AGH, ASL, MEL, RPM, HLW, WMW, BRN, MES

Competing interests: Authors declare that they have no competing interests.

Data and materials availability: All data and code are available in the Environmental Data Initiative repository (Carey et al. 2019, Carey et al. 2020, Carey et al. 2021a, Carey et al. 2021b, Carey et al. 2021e, Carey et al. 2021f) and Zenodo (Carey et al. 2021d).

Abstract

Oxygen availability is decreasing in many lakes and reservoirs worldwide, raising the urgency for understanding how anoxia (low oxygen) affects coupled biogeochemical cycling, which has major implications for water quality, food webs, and ecosystem functioning. Although the increasing magnitude and prevalence of anoxia has been documented in freshwaters globally, the challenges of disentangling oxygen and temperature responses have hindered assessment of the effects of anoxia on carbon, nitrogen, and phosphorus concentrations, stoichiometry (chemical ratios), and retention in freshwaters. The consequences of anoxia are likely severe and may be irreversible, necessitating ecosystem-scale experimental investigation of decreasing freshwater oxygen availability. To address this gap, we devised and conducted REDOX (the Reservoir Ecosystem Dynamic Oxygenation eXperiment), an unprecedented, seven-year experiment in which we manipulated and modeled bottom-water (hypolimnetic) oxygen availability at the whole-ecosystem scale in a eutrophic reservoir. Seven years of data reveal that anoxia significantly increased hypolimnetic carbon, nitrogen, and phosphorus concentrations and altered elemental stoichiometry by factors of 2-6× relative to oxic periods. Importantly, prolonged summer anoxia increased nitrogen export from the reservoir by more than seven-fold, decreased phosphorus retention, and changed the reservoir from a net sink to a net source of organic carbon downstream. While low oxygen in freshwaters is thought of as a response to land use and climate change, results from REDOX demonstrate that low oxygen is itself a *driver* of

major changes to freshwater biogeochemical cycling, which may serve as an intensifying feedback that increases anoxia in downstream waterbodies. Consequently, as climate and land use further increase the prevalence of anoxia in lakes and reservoirs globally, it is likely that anoxia will have major effects on freshwater carbon, nitrogen, and phosphorus budgets as well as water quality and ecosystem functioning.

Keywords: Biogeochemistry, Ecosystem modeling, Hypoxia, Nutrient retention, Oxygen, REDOX, Reservoir, Stoichiometry, Water quality, Whole-ecosystem experiment

Introduction

Oxygen concentrations in lakes and reservoirs around the world are decreasing, which has the potential to substantially alter freshwater ecosystem functioning and water quality. As a result of climate and land use change, low oxygen availability (anoxia) is becoming more common in the hypolimnion, or bottom waters, of many lakes and reservoirs (Jenny et al. 2016a, Jane et al. 2021, Woolway et al. 2021). An increase in both the occurrence and duration of hypolimnetic anoxia in freshwaters is likely to substantially alter the cycles of carbon (C), nitrogen (N), and phosphorus (P), three fundamental elements that determine freshwater food web structure, water quality, and ecosystem functioning (Sterner and Elser 2002). In particular, anoxia could disrupt the critical role of freshwater ecosystems as C, N, and P sinks in global biogeochemical cycles. Freshwaters retain 72% of the organic C, 56% of the total N, and 56% of the total P exported from land via sediment burial or release to the atmosphere, preventing these elements from being transported to downstream freshwater ecosystems or the oceans (Maranger et al. 2018). Altogether, the consequences of anoxia for C, N, and P concentrations,

68 stoichiometry (chemical ratios), and retention in freshwaters are likely severe and may be
69 irreversible (Nürnberg 1988, Søndergaard et al. 2003, Brothers et al. 2014, North et al. 2014),
70 necessitating ecosystem-scale investigation of how hypolimnetic anoxia affects freshwaters.
71 Biogeochemical cycles of dissolved and total C, N, and P will likely respond differently
72 to hypolimnetic anoxia (Fig. 1). In the bottom waters of lakes and reservoirs, we expect
73 dissolved organic C (DOC) concentrations to be higher in anoxic than oxic conditions, as DOC is
74 mineralized much more efficiently by oxygen than by alternate terminal electron acceptors
75 (Walker and Snodgrass 1986, Beutel 2003). Moreover, anoxia has been shown to stimulate the
76 release of DOC from sediments to the water column (Fig. 1; Brothers et al. 2014, Peter et al.
77 2017). DOC generally dominates the total OC (TOC) pool in lakes (Toming et al. 2020), thus we
78 would expect TOC to exhibit similar responses as DOC to anoxia. For hypolimnetic dissolved
79 inorganic nitrogen (DIN), ammonium (NH_4^+) concentrations would be expected to be higher in
80 anoxic conditions due to ammonification and release from sediments (Fig. 1; Rysgaard et al.
81 1994, Beutel et al. 2006). In contrast, nitrate (NO_3^-) would be lower in anoxic than oxic
82 conditions, as denitrification decreases NO_3^- in the absence of oxygen while nitrification
83 increases NO_3^- in the presence of oxygen (Fig. 1; Sharma and Ahlert 1977, Downes 1987). Total
84 nitrogen (TN) in the hypolimnion could either increase or decrease in anoxic conditions,
85 depending on the balance of NH_4^+ vs. NO_3^- within the DIN pool, as the inorganic fraction of
86 hypolimnetic dissolved N is generally greater than the organic fraction (Kim et al. 2006). For
87 hypolimnetic phosphorus (P), we would expect that dissolved reactive phosphorus (DRP)
88 concentrations would be higher in anoxic conditions as DRP is released into the water column
89 during iron reduction and particulate organic matter mineralization (Fig. 1; Boström et al. 1988,
90 Nürnberg 1988, Rydin 2000). Total P (TP) concentrations would likely exhibit a similar but

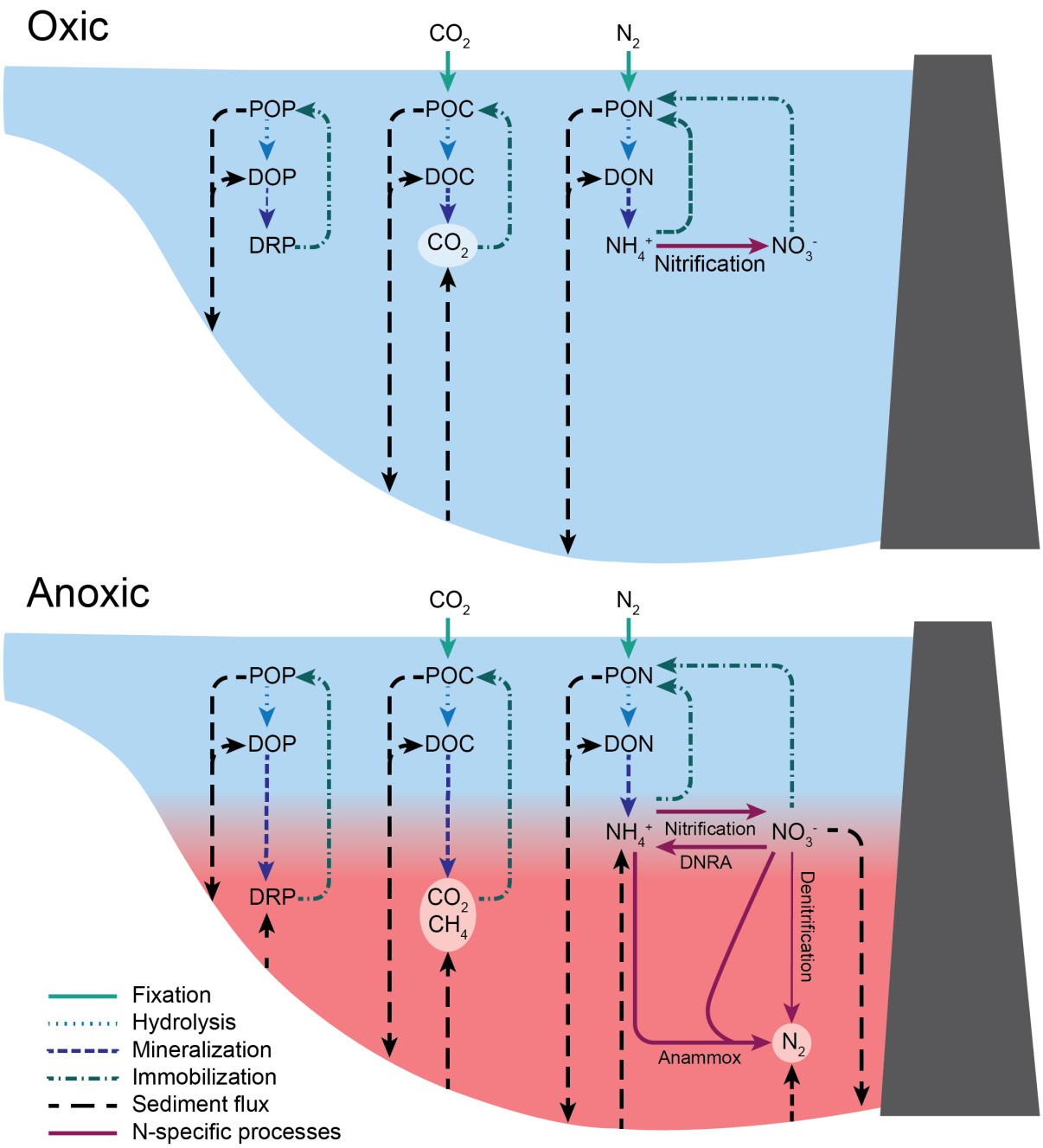

Fig. 1. Conceptual diagram of the dominant carbon, nitrogen, and phosphorus cycling processes (denoted by arrow lines) expected under oxic (top) and anoxic (bottom) conditions in the water column of a thermally-stratified reservoir. Carbon processes include cycling of carbon dioxide (CO_2), dissolved organic carbon (DOC), methane (CH_4), and particulate organic carbon (POC). Nitrogen processes include cycling of dissolved organic nitrogen (DON), nitrogen gas (N_2), ammonium (NH_4^+), nitrate (NO_3^-), and particulate organic nitrogen (PON). Phosphorus processes include cycling of dissolved organic phosphorus (DOP), dissolved reactive phosphorus (DRP), and particulate organic phosphorus (POP).

100 more muted response to anoxia than DRP, as DRP is usually a small fraction of the TP pool
101 (Wetzel 2001).

102 While these different C, N, and P processes have been well-studied individually, there
103 have been no studies on the net effect of anoxia on all of these cycles operating concurrently at
104 the ecosystem scale, likely due to the challenges of disentangling complex coupled
105 biogeochemical cycling with observational field studies or laboratory experiments. Explicitly
106 considering interconnected elemental cycles and their stoichiometry is essential to understanding
107 the effects of anoxia on ecosystem functioning (sensu Sterner and Elser 2002).

108 Increases in hypolimnetic anoxia have substantial implications for the fate of C, N, and P
109 in freshwater ecosystems. There are two primary fates for C, N, and P entering into a waterbody:
110 retention - by either remaining in the water column, burial in the sediments, or emission to the
111 atmosphere (for C and N only) - or export downstream (Tranvik et al. 2009, Beaulieu et al. 2014,
112 Powers et al. 2015, Maranger et al. 2018). Anoxia may decrease the ability of lakes and
113 reservoirs to retain NH_4^+ and DRP by reducing their burial in sediments (Rysgaard et al. 1994,
114 North et al. 2014, Powers et al. 2015), thereby increasing their downstream export. Conversely,
115 anoxia could increase the retention of NO_3^- by increasing its emission to the atmosphere via
116 denitrification (Beaulieu et al. 2014). For C, the ecosystem-scale effects of anoxia are likely
117 complex. The TOC pool includes dissolved and particulate fractions of OC that may respond to
118 oxygen differently and are mediated by ambient environmental conditions, such as external
119 loading, temperature, nutrients, and light (Hanson et al. 2015). For example, anoxia could
120 increase the retention of particulate OC (POC) by decreasing its mineralization, thereby
121 potentially increasing its burial in sediments (Walker and Snodgrass 1986, Beutel 2003).
122 Simultaneously, anoxia could decrease the retention of DOC by stimulating fluxes of DOC from

the sediments into the water column (e.g., by reductive dissolution of iron-bound DOC complexes; Skoog and Arias-Esquivel 2009), thereby potentially decreasing burial in sediments (Brothers et al. 2014, Peter et al. 2017), and increasing DOC export downstream. Consequently, quantifying the effect of anoxia on C, N, and P retention vs. export (and thus determining if a waterbody is a sink or source of C, N, and P downstream) is needed to improve our understanding of the changing role of lakes and reservoirs in global biogeochemical cycles.

In particular, human-made reservoirs, which retain substantially more inflowing C, N, and P per unit area than naturally-formed lakes globally via either sediment burial or emissions to the atmosphere (Harrison et al. 2009, Powers et al. 2016, Maranger et al. 2018), may be very sensitive to the effects of hypolimnetic anoxia. Despite only covering 6-11% of the global lentic surface (Downing et al. 2006, Lehner et al. 2011, Verpoorter et al. 2014), reservoirs alone are estimated to account for ~40% of total annual global OC burial (Mendonça et al. 2017) and 26% of total annual global P burial (Maranger et al. 2018). Moreover, reservoirs globally emit 6.5 Tg N yr^{-1} to the atmosphere, primarily via denitrification (Harrison et al. 2009, Beusen et al. 2016). In an analysis of ~1000 lakes and reservoirs sampled once across the U.S., reservoirs were found to have lower organic C:P and N:P ratios than naturally-formed lakes, which was attributed in part to a greater incidence of hypolimnetic anoxia in reservoirs than naturally-formed lakes (Maranger et al. 2018). However, that study lacked accompanying oxygen data to examine how C, N, and P varied across a gradient of oxygen availability. Moreover, the amalgamation of data from waterbodies with different climate and catchment land use makes it challenging to quantify how changing oxygen alters water column C, N, and P concentrations, stoichiometry, and export. To mechanistically quantify the effects of anoxia on C, N, and P cycling, we need new approaches that embrace the dynamical nature of reservoirs over time and allow us to disentangle

146 the effects of hypolimnetic anoxia on these waterbodies, especially as their construction is
147 increasing globally (Zarfl et al. 2015).

148 Coupled whole-ecosystem manipulations and ecosystem modeling provide a powerful
149 approach for both quantifying the effects of hypolimnetic anoxia on C, N, and P cycling and
150 testing the mechanisms underlying continental-scale patterns derived from thousands of
151 waterbodies (e.g., Helton et al. 2015, Maranger et al. 2018). Foundational work based on
152 sediment core incubations in the laboratory and small chambers placed in situ on the sediments
153 of lakes and reservoirs (e.g., Frindte et al. 2015, Lau et al. 2016) have yet to be tested at the
154 ecosystem scale, which is needed to overcome the limitations of small volumes of water and
155 mesocosm fouling. Studies that manipulate an entire ecosystem are able to disentangle the effects
156 of oxygen availability from other environmental drivers, such as water temperature and
157 biological activity, on C, N, and P cycling. However, it is logistically challenging to replicate
158 these intensive experiments under different meteorological and environmental conditions over
159 time to assess robustness and repeatability of ecosystem responses. Consequently, data from
160 whole-ecosystem manipulations can be used to calibrate ecosystem models (following Medlyn et
161 al. 2015) that can simulate complex ecosystem responses under a range of oxygen scenarios and
162 weather conditions over multiple years, thereby overcoming the constraints of separate empirical
163 and model investigations.

164 We devised and conducted REDOX (the Reservoir Ecosystem Dynamic Oxygenation
165 eXperiment), an unprecedented, seven-year study that integrated a long-term hypolimnetic
166 oxygenation manipulation with ecosystem modeling in a eutrophic reservoir. The purpose of
167 REDOX was to study ecosystem-scale functioning under contrasting oxygen conditions over
168 multiple years. First, we intensively monitored dissolved oxygen and total and dissolved C, N,

and P chemistry, as well as a suite of accompanying water quality variables, in the reservoir during the seven-year field manipulation. Second, we used the empirical data to calibrate a coupled hydrodynamic-ecosystem model, which was used to quantify the effects of varying oxygen conditions over the seven years. To investigate further changes in reservoir C, N, and P and carbon cycling due to anoxia, we used the calibrated model to test hypolimnetic oxygen scenarios under a range of seasonal and meteorological conditions. We focused on two contrasting model scenarios: one in which there was oxygenation throughout the stratified summer periods in all seven years, resulting in continuous oxic conditions, and one in which there was no oxygenation, resulting in hypolimnetic anoxia every summer. We used the model output to address the following questions: 1) How does hypolimnetic oxygen availability affect total and dissolved C, N, and P concentrations and stoichiometry?, and 2) How does hypolimnetic anoxia affect reservoir retention and downstream export of C, N, and P?

Materials and Methods

Site description

We studied the effect of changing oxygen conditions on C, N, and P dynamics in Falling Creek Reservoir (FCR), a small eutrophic reservoir located in Vinton, Virginia, USA (37.303479,-79.837371; Fig. 2). FCR has a maximum depth of 9.3 m and surface area of 0.119 km^2 and is a drinking water source operated by the Western Virginia Water Authority (WVWA; Gerling et al. 2014). FCR's watershed was farmland at the time of reservoir construction in 1898 and is almost completely deciduous forest today following agricultural abandonment in the 1930s (Gerling et al. 2016). The reservoir has never been dredged (Gerling et al. 2016), and had a mean hydraulic residence time of 281 days (±12 days, 1 S.E.) during our study.

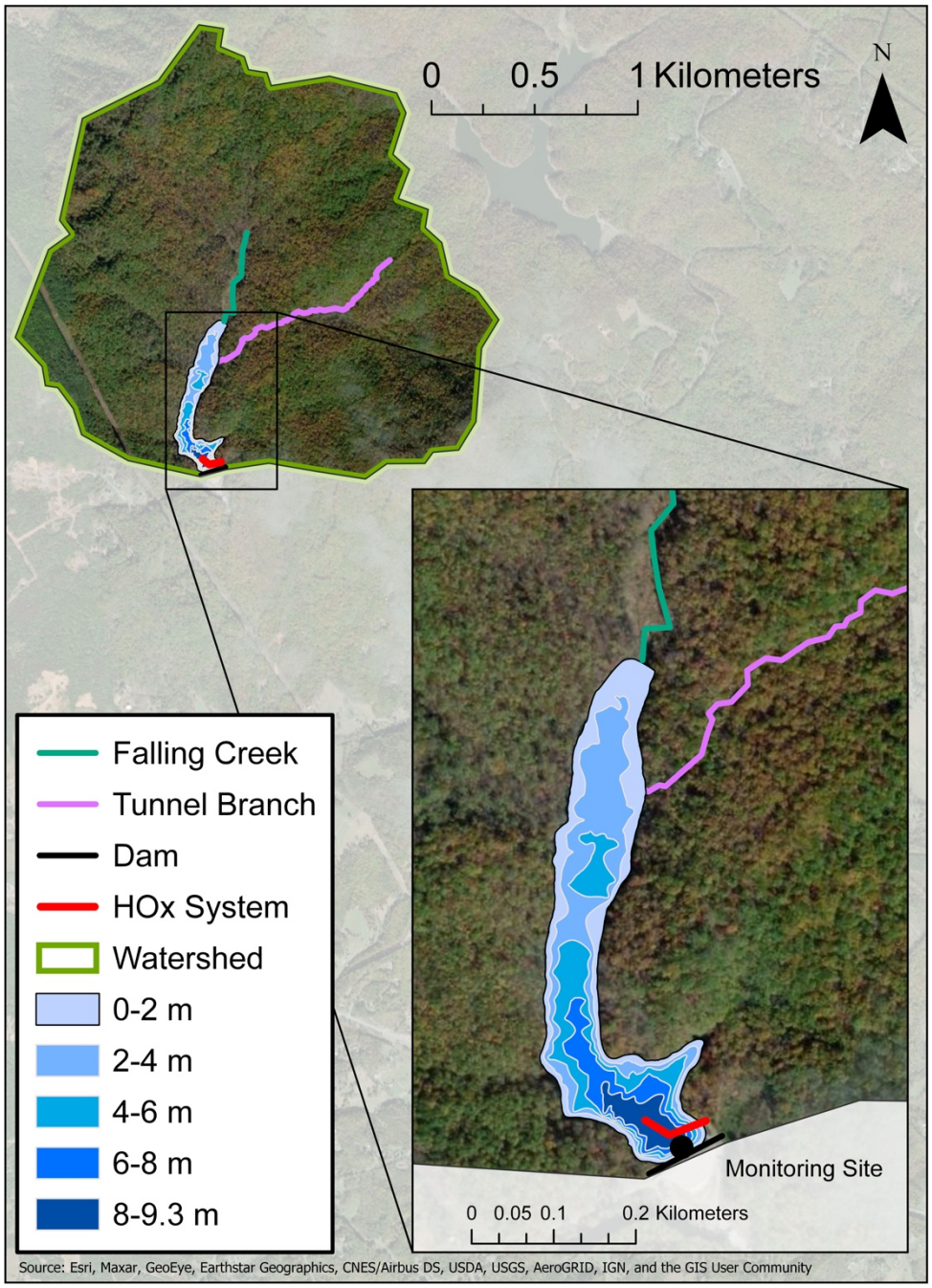

Fig. 2. Map of Falling Creek Reservoir, Vinton, VA, USA (37.303479, -79.837371). The map shows the reservoir watershed, locations of the two inflow streams (Falling Creek and Tunnel Branch), dam, hypolimnetic oxygenation (HOx) system, and monitoring site near the dam.

Whole-ecosystem manipulations

We manipulated hypolimnetic oxygen availability in FCR using an engineered hypolimnetic oxygenation system (HOx) deployed by the WVWA in 2012, which allowed us to generate contrasting summer oxic and anoxic conditions (Gerling et al. 2014). The HOx system withdraws hypolimnetic water from 8 m depth, injects dissolved oxygen into the water at super-saturated concentrations onshore, and returns the oxygenated water back to the hypolimnion at 8 m without altering thermal stratification or water temperature (Gerling et al. 2014).

During summers in 2013-2019, the HOx system was operated at variable oxygen addition levels and durations in collaboration with the WVWA (Carey et al. 2021d). Some summers experienced intermittent 2–4 week periods of oxygenation (2013, 2014, 2019); some summers had near-continuous oxygenation (2015, 2016, 2017), and one summer had approximately half oxygenation (2018; Carey et al. 2021d). These wide-ranging oxygenation conditions, which occurred because the reservoir was an actively-managed drinking water source, provided an ideal dataset for calibrating the biogeochemical rates in the ecosystem model to variable hypolimnetic oxygen conditions, as described below.

Monitoring data

FCR's physics, chemistry, and biology were intensively monitored throughout the REDOX manipulations (see Supplementary Text 1 for detailed sampling methods). On every sampling day, depth profiles of water temperature and dissolved oxygen were collected at the deepest site of the reservoir, near the dam (Carey et al. 2021b). We collected water samples for total and dissolved C, N, and P analysis from the reservoir's water treatment extraction depths (0.1, 1.6, 2.8, 3.8, 5.0, 6.2, 8.0, and 9.0 m) using a Van Dorn sampler. Water was filtered through

glass-fiber 0.7 micron filters into acid-washed bottles and immediately frozen until analysis for dissolved C, N, and P samples (Carey et al. 2021e). Unfiltered water was frozen in separate acid-washed bottles for total samples (Carey et al. 2021e).

We used standard methods for biogeochemical analyses (see Supplementary Text 2 for detailed laboratory methods). We used flow injection analysis to determine concentrations of N and P colorimetrically (APHA 2017), with an alkaline persulfate digestion for TN and TP fractions. DOC and TOC were determined by either heated persulfate digestion or high-temperature combustion followed by infrared absorbance (APHA 2017). All field and laboratory data are available with metadata in the Environmental Data Initiative (EDI) repository (Carey et al. 2019, Carey et al. 2020, Carey et al. 2021a, Carey et al. 2021b, Carey et al. 2021e, Carey et al. 2021f).

Model description and driver data

We used the empirical data to calibrate and validate the General Lake Model coupled to Aquatic EcoDynamics modules (GLM-AED, v.3.2.0a3) configured for FCR (see Supplementary Text 3 for detailed modeling methods). GLM-AED is an open-source, 1-D numerical simulation model that is widely used in the freshwater research community to model lakes and reservoirs (e.g., Bruce et al. 2018, Hipsey et al. 2019, Farrell et al. 2020, Ward et al. 2020). GLM-AED requires meteorological, inflow, and outflow driver data and simulates water balance and thermal layers using a Lagrangian strategy (Hipsey et al. 2019). GLM-AED has a flexible structure in which modules representing different ecosystem components can be turned on or off to recreate varying levels of ecosystem complexity; our configuration for FCR included modules for oxygen, C, silica (Si), N, P, organic matter, and phytoplankton (Carey et al. 2021c).

GLM-AED simulates the dominant processes controlling freshwater oxygen and C, N, and P cycling (see Supplementary Text 3; Farrell et al. 2020, Ward et al. 2020). Biogeochemical processes (e.g., sediment fluxes, mineralization) were modeled as a function of both oxygen following Michaelis-Menten dynamics and temperature following Arrhenius coefficients (Farrell et al. 2020). Consequently, processes that are favored in anoxic conditions (e.g., sediment fluxes of DOC, NH_4^+, and DRP into the hypolimnion) were still simulated in oxic conditions, but at much lower rates.

The ecosystem model provided important insight on the effects of anoxia that would have been impossible to obtain from the field manipulation alone. First, while we do report on the biogeochemical responses to the field manipulation, ecosystems rarely experience such rapid shifting of redox conditions at sub-seasonal scales, as were created by abrupt additions of oxygen via the HOx system. Thus, to understand how our FCR results applied to other waterbodies, we used the seven-year field manipulation as a proxy to contrast the consequences of seasonally-oxic vs. anoxic hypolimnia for biogeochemical cycling in an ecosystem model. These highly contrasting scenarios were achieved in the model by manipulating hypolimnetic oxygen injection (described below). Second, to determine the cumulative fate of C, N, and P over an entire summer in response to oxygen dynamics, it is important to track these elements at a high temporal resolution. Because our field data were collected weekly to monthly, we used numerical modeling of hydrodynamics and ecosystem processes to capture daily dynamics. Third, the field manipulation included a variable oxygenation schedule which occurred against a backdrop of changing meteorology and hydrology. Consequently, the model enabled us to isolate the effects of oxygen availability on the reservoir's biogeochemistry and evaluate the robustness of ecosystem responses across varying environmental conditions.

Model configuration and calibration

All GLM-AED model configuration files, parameters, and driver data for FCR are available in the EDI repository (Carey et al. 2021c). GLM-AED driver data included hourly meteorological data from NASA's North American Land Data Assimilation System (NLDAS-2; Xia et al. 2012), stream inflow data, and outflow data. We developed stream inflow driver datasets - which consisted of daily discharge, water temperature, and chemistry - for the two primary streams entering FCR from observational data (Supplementary Text 3). To simulate the HOx system in the model, we added a submerged inflow that injected oxygenated water into the reservoir at 8 m, the same depth as in the reservoir (Supplementary Text 3). As the reservoir was managed to keep constant water level, outflow volume was set to equal inflow volume; the physical and chemical properties of the outflow were determined by the state of the modeled reservoir (Supplementary Text 3).

We ran the model from 15 May 2013 to 31 December 2019, divided into calibration (15 May 2013-31 December 2018) and validation (1 January 2019-31 December 2019) periods for model verification. GLM-AED was run on an hourly time step throughout the total simulation period (Carey et al. 2021c).

We calibrated GLM-AED to observed conditions (Supplementary Text 3). First, we conducted a global sensitivity analysis to identify the most important parameters for simulating water temperature, dissolved oxygen, NH_4^+, NO_3^-, DRP, and DOC following (Morris 1991). Second, we calibrated the identified sensitive parameters (Supplementary Text 3) using the covariance matrix adaptation evolution strategy for automated numerical optimization to minimize root mean square error (RMSE) between observations and model output (Hansen 2016) for all sampling depths in the water column.

We calculated multiple goodness-of-fit metrics to assess the model's performance during the calibration period, validation period, and total simulation period, including RMSE, percent bias, Nash-Sutcliffe (NSE), normalized mean absolute error (NMAE), and Pearson's correlation coefficient (Kara et al. 2012, Ward et al. 2020, Ladwig et al. 2021). We focus on hypolimnetic concentrations below but present model output and goodness-of-fit metrics for the full water column in Supplementary Text 4.

Model scenarios

Following model calibration, we examined the effects of two different oxygen scenarios on the calibrated GLM-AED model: one in which the model was forced with a high level of oxygenation to keep the hypolimnion oxic throughout summer thermal stratification (May 15-Oct 15) during 2013-2019 and one in which zero oxygen was added to the hypolimnion, so hypolimnetic anoxia quickly set up after the onset of thermal stratification each summer. All other driver data (meteorology, stream inflows, outflow) were held constant.

Statistical analysis

We used several approaches to answer the two research questions. For Q1, we first compared observed data from the oxygenated vs. non-oxygenated periods of our field manipulation to determine if oxygenation had an effect on empirical total and dissolved C, N, and P concentrations. We also used the FCR field data to validate the model's ability to simulate the field manipulation. Second, because our goal was to compare completely oxic vs. completely anoxic summers and every summer had at least some oxygenation during the seven-year field manipulation, we focused our subsequent analyses on the anoxic vs. oxic model scenario output,

311 not the observational data. Focusing on the model output for this analysis also enabled us to
312 overcome the limitations of comparing years with different numbers of sampling observations, as
313 the model calculated daily C, N, and P concentrations and rates.
314 We compared hypolimnetic C, N, and P concentrations and rates between the oxic and
315 anoxic model scenarios during 15 July - 1 October among years, the interval within the summer
316 thermally-stratified period when the reservoir consistently exhibited hypolimnetic anoxia in non-
317 oxygenated conditions. We calculated the median hypolimnetic dissolved and total
318 concentrations of C, N, and P during this period for each of the seven years (2013-2019), and
319 compared the median summer anoxic and oxic concentrations and their ratios using paired t-
320 tests, as there was no temporal autocorrelation among median summer values. We also examined
321 summer rates of all processes controlling increases and decreases in hypolimnetic C, N, and P to
322 determine their relative importance and sensitivity to oxygen.
323 For Q2, we estimated C, N, and P downstream export as a percent of inputs into the
324 reservoir each summer (Powers et al. 2015, Farrell et al. 2020). Downstream export was
325 calculated as:
326 $Flux = 100\% \times (\Sigma\, Outputs - \Sigma\, Inputs)/\Sigma\, Inputs)$ (eqn. 1)
327 where Outputs and Inputs represent the daily mass of C, N, or P leaving and entering the
328 reservoir, respectively, during 15 July - 1 October each year. Fluxes were calculated for both
329 dissolved and total fractions of C, N, and P. Inputs were calculated by multiplying the individual
330 stream daily inflow concentrations with their daily inflow volumes and then summing across the
331 two streams. Outputs were calculated by multiplying the outflow water volume (leaving the
332 reservoir and going downstream) by hypolimnetic concentrations. Inputs and Outputs were
333 summed across the 15 July - 1 October period to calculate flux, so that flux values of 0 indicated

that the reservoir inputs balanced outputs; flux values <0 indicated that the reservoir was a net sink of C, N, or P; and flux values >0 indicated that the reservoir was a net source of C, N, or P downstream. We compared summer retention (i.e., flux values) in the anoxic and oxic scenarios with paired t-tests. To ease comparison among C, N, and P concentrations and ratios, all analyses were conducted using molar units. All modeling analyses were conducted in R v.3.6.3 (R Core Team 2020).

Results

Our integrated whole-ecosystem REDOX field manipulation and modeling demonstrates that hypolimnetic anoxia significantly alters water column C, N, and P concentrations and stoichiometry. Importantly, our study also shows that prolonged hypolimnetic anoxia in the summer decreases the ability of a reservoir to retain C, N, and P, substantially increasing its downstream export.

Observational data from whole-ecosystem manipulations

Injection of oxygen into the bottom waters of Falling Creek Reservoir (FCR) over seven years increased the reservoir's observed hypolimnetic oxygen, resulting in substantial changes in total and dissolved C, N, and P concentrations (Fig. 3). Due to the nature of our oxygenation manipulation, some years experienced limited oxygenation (e.g., oxygenation was turned on and off throughout the summer), while some experienced full oxygenation for the duration of the stratified period (Fig. 3B). During the summers with limited oxygenation (2014, 2018, 2019), observed hypolimnetic DOC, TN, NH_4^+, TP, and DRP concentrations were higher than in summers with continuous oxygenation (2015, 2016, and 2017; Fig. 3C,D,E,G,H). Conversely,

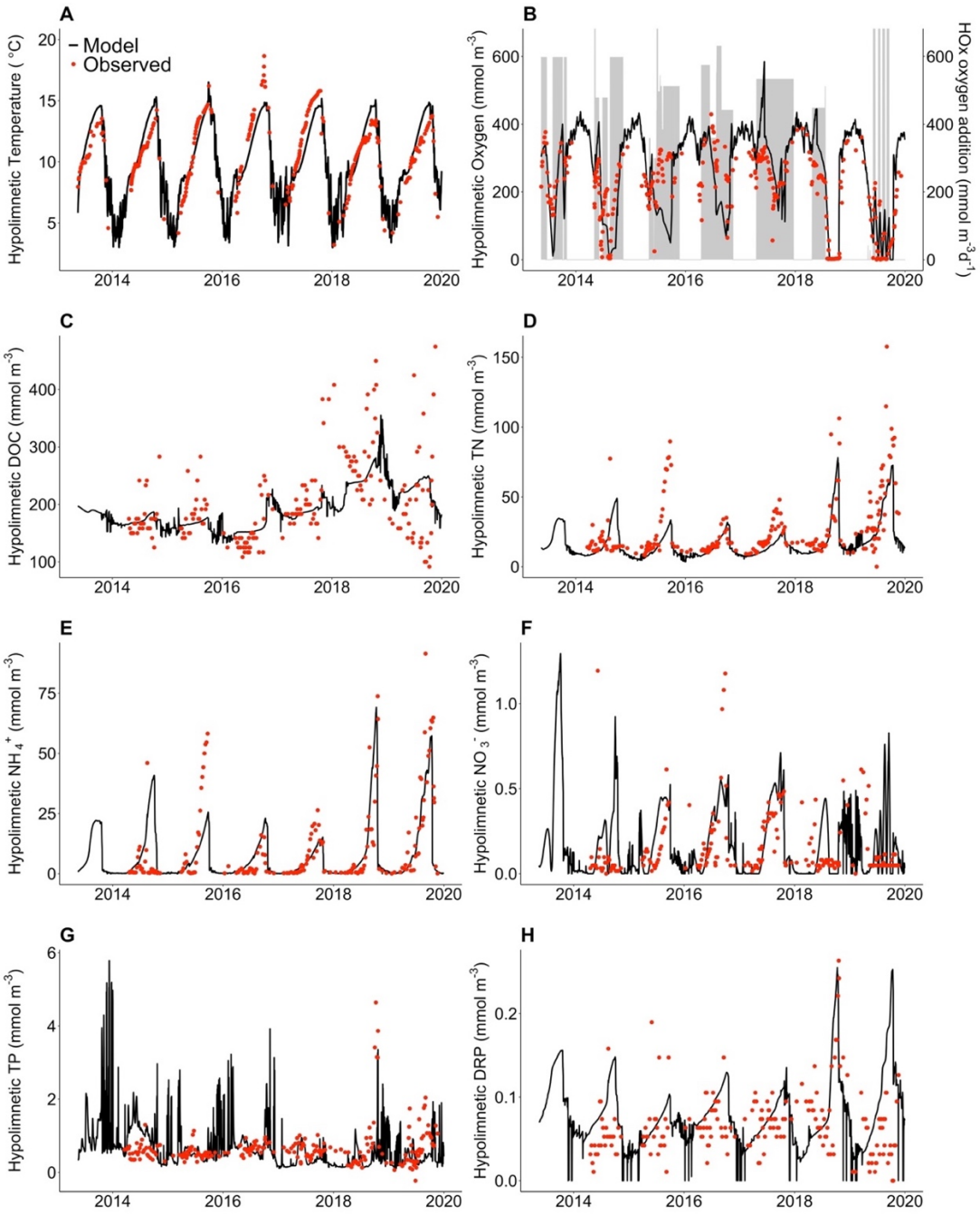

Fig. 3. The model was able to recreate observed reservoir dynamics. Modeled (black line) and observed (red points) hypolimnetic (9 m) water temperature (A), dissolved oxygen (B), dissolved organic carbon (DOC; C), total nitrogen (TN; D), ammonium (NH_4^+; E), nitrate (NO_3^-; F), total phosphorus (TP; G), and dissolved reactive phosphorus (DRP; H) in Falling Creek Reservoir. The grey shaded areas in panel B represent the periods and addition rates of oxygen injection into the hypolimnion from the hypolimnetic oxygenation system (HOx) during the seven-year field manipulation. Note varying y-axes among panels, and that most of the TP and DRP observations were below the limit of quantitation in laboratory analysis (0.15 and 0.08 mmol m^{-3}, respectively).

maximum observed hypolimnetic NO_3^- concentrations were lower in summers with limited oxygenation than summers with continuous oxygenation (Fig. 3F). Thermal stratification and hypolimnetic water temperature in the reservoir were not noticeably affected by oxygenation (Fig. 3A). Because our goal was to compare completely oxic vs. completely anoxic summer conditions and every summer had at least some oxygenation during the seven-year field manipulation, subsequent analyses focused on the anoxic vs. oxic model scenario output, described below.

The field manipulation data were used to calibrate the ecosystem model, which was able to reproduce observed C, N, and P concentrations and stoichiometry (Fig. 3). The goodness-of-fit metrics for water temperature, oxygen, water chemistry concentrations, and stoichiometric ratios over the 2013-2019 simulation period (Supplementary Text 4) were all within reported ranges for lake ecosystem numerical simulation models (e.g., Kara et al. 2012, Farrell et al. 2020, Ward et al. 2020, Ladwig et al. 2021). Similar to field observations, the simulation of oxygen injection in the model did not substantively alter modeled water temperature (Fig. 3A) or thermocline depth (Supplementary Text 4).

How does hypolimnetic oxygen availability affect total and dissolved C, N, and P concentrations and stoichiometry?

Model scenarios show that hypolimnetic anoxia significantly affected all three focal elemental cycles, but that N was the most sensitive (Figs. 4,5; see Supplementary Text 5 for statistics). Summer TN molar concentrations in the reservoir were on average 3.3× higher in anoxic than oxic conditions, relative to a 1.1× increase of TOC and 1.3× increase of TP (Fig. 5A,C,G). The dissolved fractions accounted for most of the changes in total C, N, and P: during

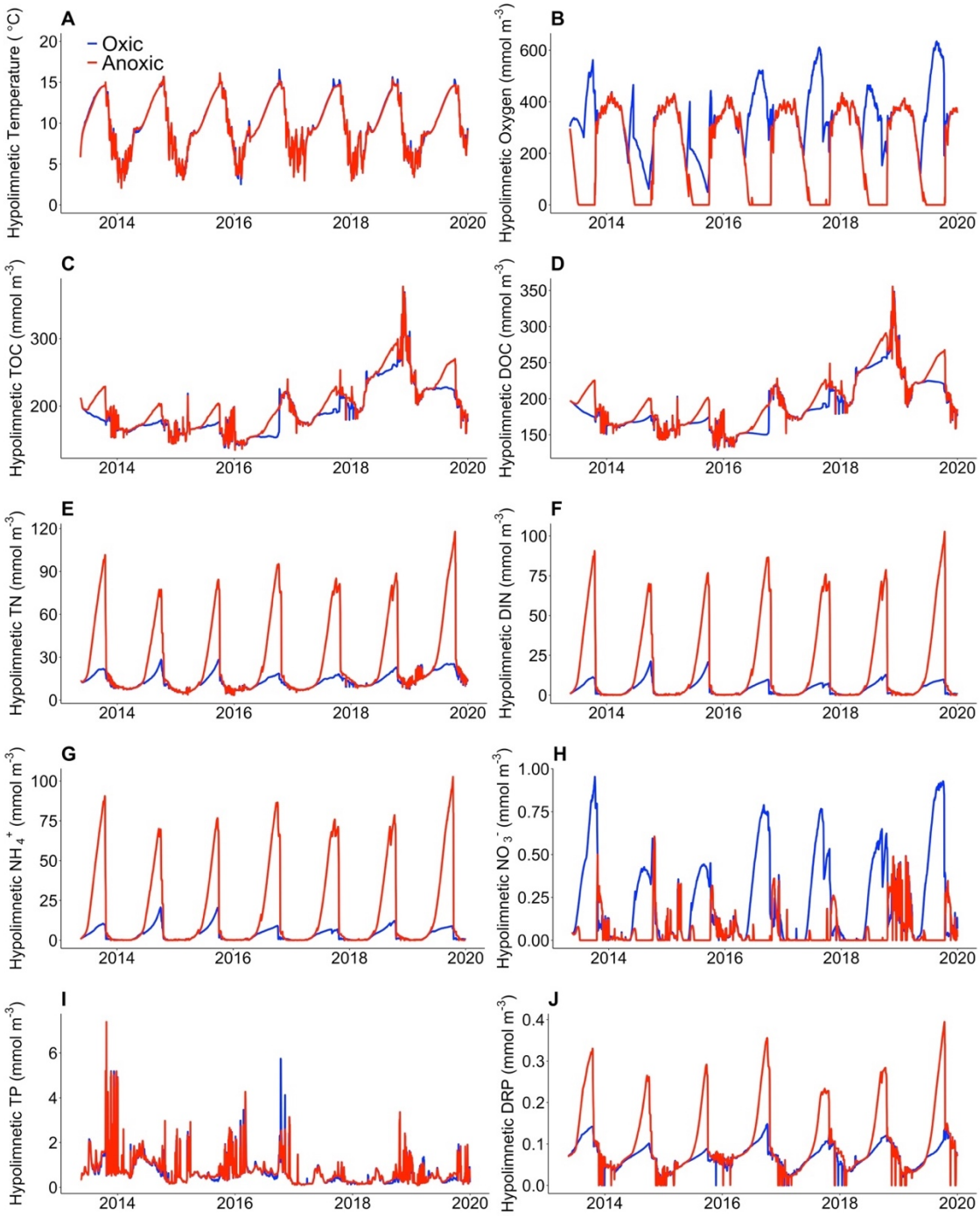

Fig. 4. Time series of oxic (blue) and anoxic (red) model scenarios in Falling Creek Reservoir. Model results are shown for hypolimnetic (9 m) water temperature (A), dissolved oxygen (B), total organic carbon (TOC; C), dissolved organic carbon (DOC; D), total nitrogen (TN; E), dissolved inorganic nitrogen (DIN, the sum of ammonium and nitrate; F), ammonium (NH_4^+; G), nitrate (NO_3^-; H), total phosphorus (TP; I), and dissolved reactive phosphorus (DRP; J). In the oxic scenario, oxygen was injected into the hypolimnion throughout the thermally-stratified period each summer. In the anoxic scenario, no oxygen was added to the hypolimnion, resulting in prolonged hypolimnetic anoxia each summer. Note varying y-axes among panels.

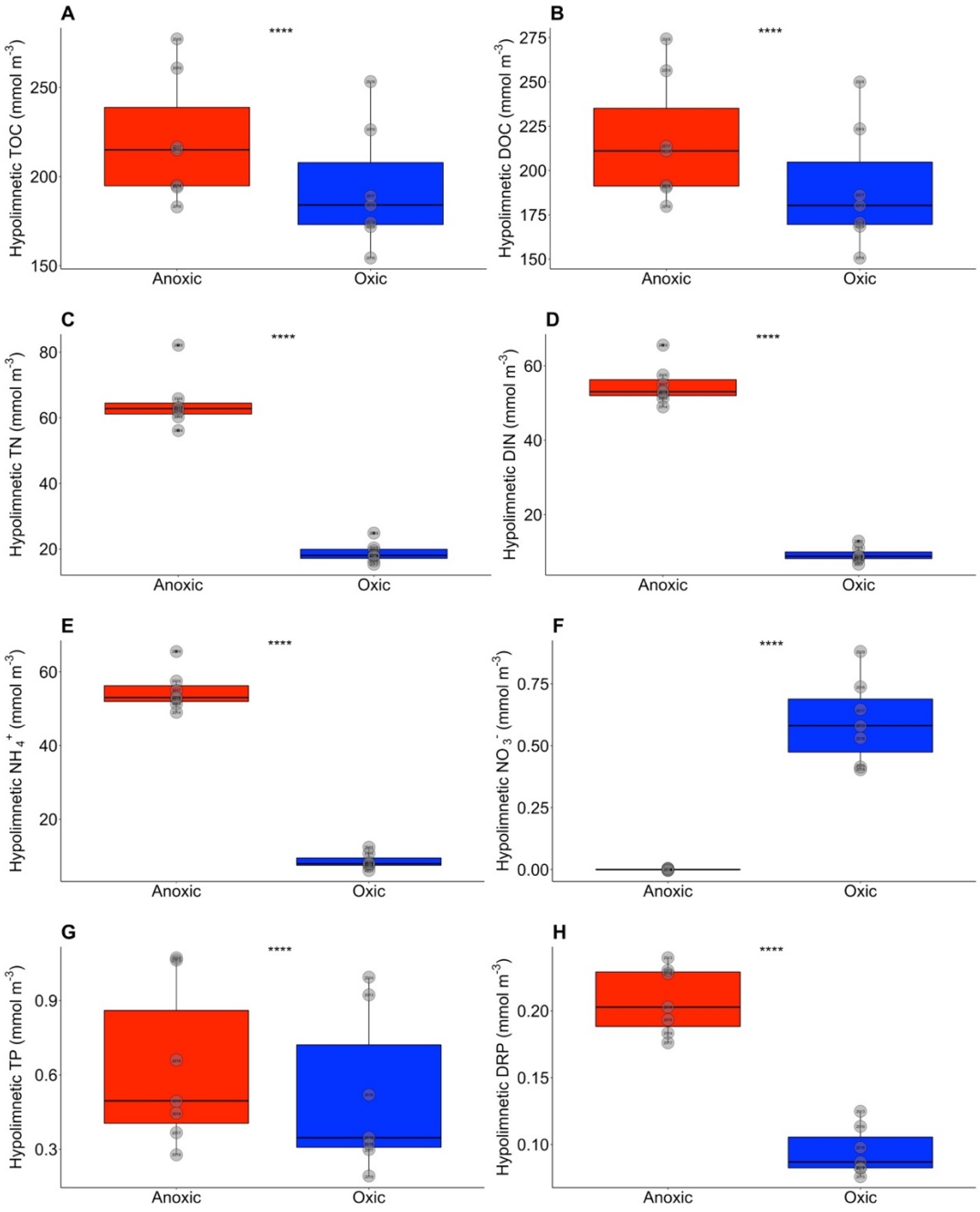

Fig. 5. Anoxia significantly altered bottom-water concentrations of carbon, nitrogen, and phosphorus. Median hypolimnetic (9 m) total organic carbon (TOC; A), dissolved organic carbon (DOC; B), total nitrogen (TN; C), dissolved inorganic nitrogen (DIN; D), ammonium (NH_4^+; E), nitrate (NO_3^-; F), total phosphorus (TP; G), and dissolved reactive phosphorus (DRP; H) concentrations between anoxic (red) and oxic (blue) scenarios during Falling Creek Reservoir's stratified period (July 15 - October 1) for all years of this study. The grey points are the median values from each of the seven years. The **** denotes that the difference between the median summer anoxic and oxic scenario concentrations was highly statistically significant (all paired t-tests $p \leq 0.0001$, see Supplementary Text 5 for statistics). Note varying y-axes among panels.

411 anoxic conditions, summer hypolimnetic DOC, NH_4^+, and DRP concentrations in FCR were on
412 average 1.1, 6.4, and 2.1× higher, respectively, than in oxic conditions (Fig. 5B,E,H).
413 Conversely, hypolimnetic NO_3^- was much lower in anoxic conditions (usually at or just above 0
414 mmol m^{-3}) than oxic conditions, but DIN exhibited an overall increase because of the dominance
415 of NH_4^+ over NO_3^- in the dissolved inorganic N pool (Fig. 5D,F).

416 The elemental stoichiometry in FCR exhibited rapid and large ecosystem-scale changes
417 after the onset of anoxia each summer. While total and dissolved fractions of C, N, and P (except
418 NO_3^-) significantly increased with anoxia (Figs. 4,5), the different fractions had varying
419 sensitivities to changing oxygen, resulting in significant changes in C, N, and P ratios (Fig. 6,
420 Supplementary Text 5). Hypolimnetic TN:TP and DIN:DRP were significantly higher (on
421 average, by 2.6× and 2.9×, respectively) in anoxic conditions than oxic conditions (Fig. 6G,H).
422 Because modeled hypolimnetic NO_3^- concentrations were at or near zero during anoxic
423 conditions (Fig. 5F), DOC:NO_3^- could not be consistently calculated (Fig. 6E). In contrast,
424 TOC:TN, DOC:DIN, DOC:NH_4^+, and DOC:DRP were significantly higher (on average, by 2.9×,
425 5.2×, 5.6×, and 1.9×, respectively) in oxic conditions than anoxic conditions (Fig. 6A,C,D,F).
426 TOC:TP was the only ratio of those examined that did not show a significant response to anoxia
427 (Fig. 6B, Supplementary Text 5).

428 The most important processes driving the biogeochemical responses to anoxia were much
429 higher fluxes of NH_4^+, DRP, and DOC from the sediments into the hypolimnion relative to oxic
430 periods (Fig. 7). During anoxic summer conditions, the median release rates of NH_4^+ and DRP
431 from the sediments into the water column were 4.0× and 1.7× higher, respectively, than in oxic
432 conditions (Fig. 7). During oxic conditions, the sediment release rate of NH_4^+ into the
433 hypolimnion was 36× greater than the consumption of NH_4^+ by nitrification (Fig. 7), thereby

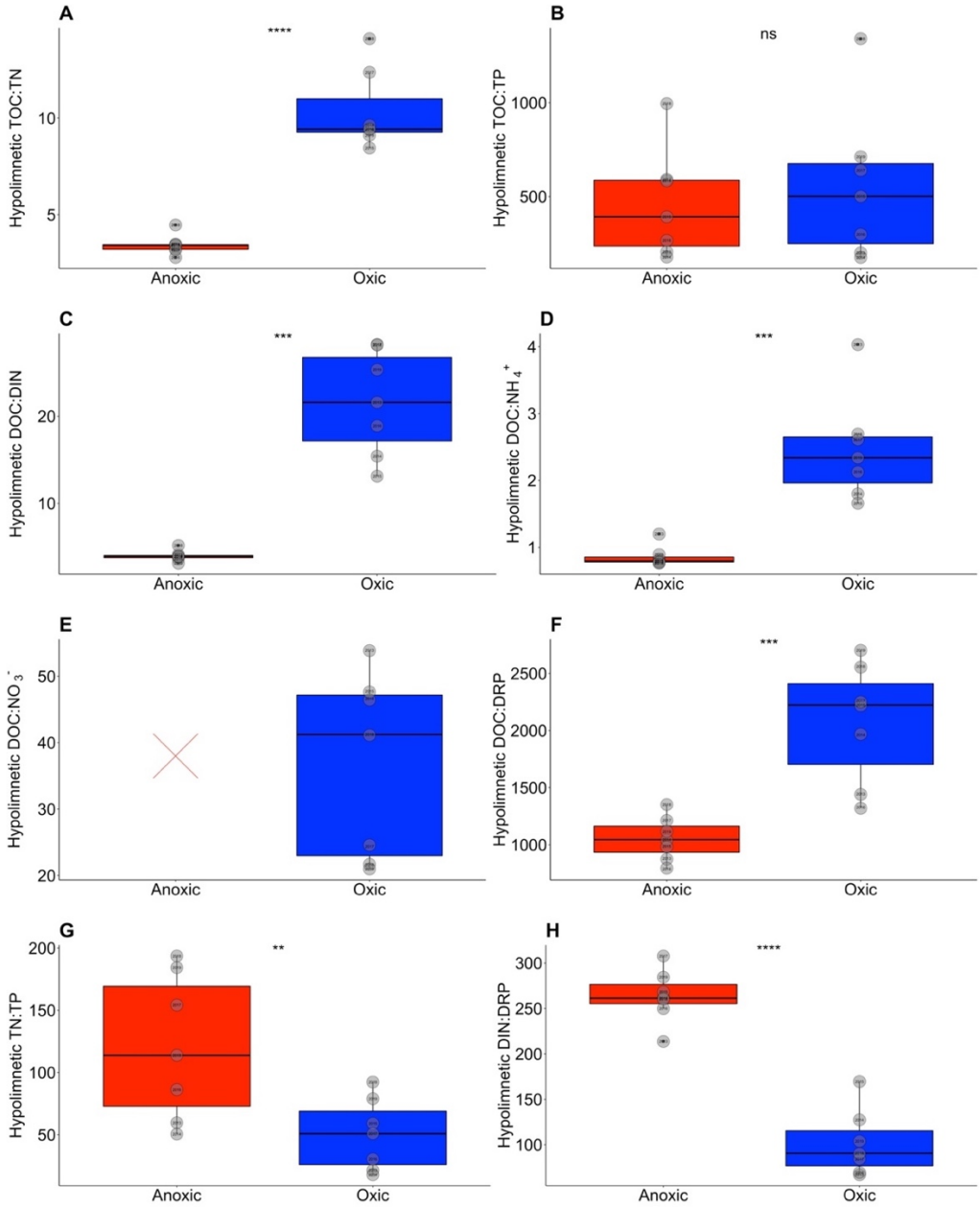

Fig. 6. Anoxia significantly affected water column stoichiometry. Total and dissolved molar ratios of hypolimnetic (9 m) total organic carbon:total nitrogen (TOC:TN; A), TOC:total phosphorus (TOC:TP; B), dissolved organic carbon:dissolved inorganic nitrogen (DOC:DIN; C), DOC:ammonium ($DOC:NH_4^+$; D), DOC:nitrate ($DOC:NO_3^-$; E), DOC:dissolved reactive phosphorus (DOC:DRP; F), TN:TP (G), and DIN:DRP (H) between anoxic (red) and oxic (blue) scenarios during Falling Creek Reservoir's stratified period (July 15 - October 1) for all years of this study. The grey points are the median values from each of the seven years. Because NO_3^- concentrations in the anoxic scenario were functionally zero, the ratio of $DOC:NO_3^-$ could not be calculated (hence the X in panel E). The asterisks denote the p-values from paired t-tests comparing the median summer ratios between anoxic and oxic scenarios: **** $p < 0.0001$, *** $p < 0.001$, ** $p < 0.01$, * $p < 0.05$, and ns (not significant) $p \geq 0.05$ (see Supplementary Text 5 for statistics). Note varying y-axes among panels.

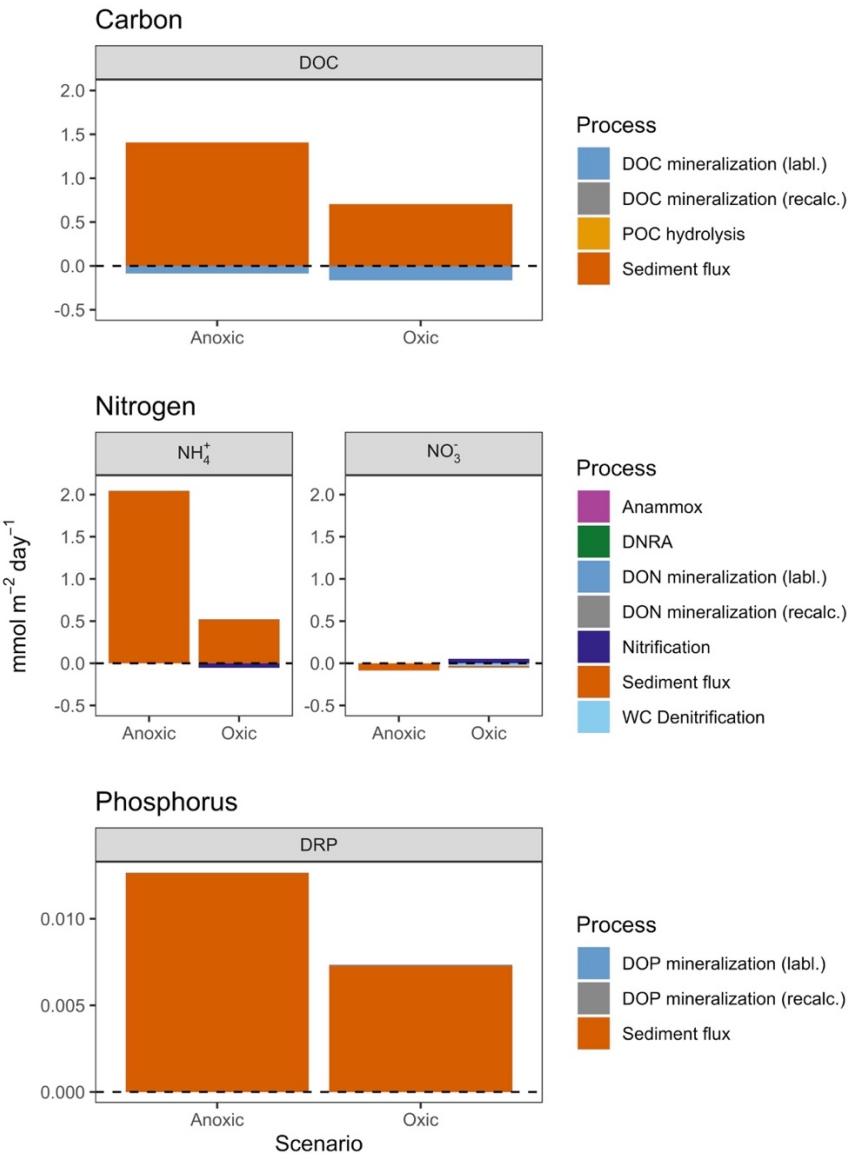

Fig. 7. The rates of the dominant processes altering the biogeochemical cycling of dissolved carbon, nitrogen, and phosphorus changed in response to anoxia. Comparison of the dominant biogeochemical processes altering dissolved pools of carbon (dissolved organic carbon, DOC; top), nitrogen (ammonium, NH_4^+, and nitrate, NO_3^-; middle), and phosphorus (dissolved reactive phosphorus, DRP; bottom) in the hypolimnion of Falling Creek Reservoir under anoxic vs. oxic model scenarios. Rates shown represent the median contribution of each process to hypolimnetic concentrations of DOC, NH_4^+, NO_3^-, and DRP during Falling Creek Reservoir's summer stratified period (July 15 - October 1) for all years of this study. Positive rates indicate that the process increased hypolimnetic concentrations; negative rates indicate that the process decreased hypolimnetic concentrations. Mineralization is shown separately for both labile (labl.) and recalcitrant (recalc.) dissolved organic pools, and denitrification is partitioned for the water column (WC Denitrification) and sediment in the NO_3^- panel (Sediment flux). Note the varying y-axes among panels and that some rates are so small that they are not visible in the figure.

462 explaining the hypolimnetic accumulation of NH_4^+ that occurred during oxic conditions (Fig.
463 4G). Although median labile dissolved organic N (DON) and P (DOP) mineralization rates were
464 3.7× and 3.9× times higher in oxic than anoxic conditions, respectively, their contribution to
465 hypolimnetic N and P budgets was much smaller than NH_4^+ and DRP sediment fluxes. All
466 biogeochemical rates involving the cycling of NO_3^- were much lower than for NH_4^+ overall,
467 likely because of the much lower concentrations of NO_3^- within the DIN pool. For DOC, the
468 median sediment fluxes increasing DOC in the hypolimnion were 2.1× times higher in anoxic
469 than oxic conditions. Although labile DOC mineralization rates were 2.0× higher in oxic than
470 anoxic conditions, sediment flux rates were 18× higher than mineralization rates, resulting in
471 much greater hypolimnetic accumulation of DOC in anoxic relative to oxic periods (Fig. 7).
472 The time scales at which C, N, and P concentrations responded to shifts in hypolimnetic
473 oxygen availability differed as a result of multiple interacting biogeochemical processes (Figs.
474 4,7). For example, the onset of anoxia resulted in rapid decreases in NO_3^- (Fig. 4H), due to
475 sediment denitrification oxidizing NO_3^- to N_2 (Fig. 7). Similarly, the rapid increases in
476 hypolimnetic NH_4^+ and DOC concentrations after the onset of anoxia (Fig. 4D,G) were
477 attributable to the high rates of NH_4^+ and DOC sediment release (Fig. 7). In comparison,
478 hypolimnetic DRP accumulation in response to anoxia occurred more slowly (Fig. 4J). This
479 difference in time scale reflects the lower fitted value of the half-saturation constant of modeled
480 DRP sediment fluxes (6.91 mmol m^{-3}) relative to the half-saturation constants of NH_4^+ sediment
481 fluxes (41.25 mmol m^{-3}) and DOC sediment fluxes (93.13 mmol m^{-3}) (Carey et al. 2021c).
482 Consequently, oxygen concentrations in the hypolimnion had to decrease to near zero before
483 anoxia stimulated an increase in DRP sediment fluxes, following Michaelis-Menten dynamics.
484

How does hypolimnetic anoxia affect reservoir downstream export of C, N, and P?

Overall, anoxia significantly increased downstream export of C, N, and P from FCR (Fig. 8). During the summer months, if the reservoir's hypolimnion was oxic, FCR served as a sink for inflowing TOC, TP, DOC, and DRP, decreasing the downstream export of those fractions (Fig. 8A,B,G,H). The reservoir served as a particularly important TP sink during summer oxic conditions, with 90% of inflowing TP buried in sediments and only 10% of the inflow TP exported downstream (Fig. 9). The reservoir was still a TP sink during anoxic conditions, but slightly more inflowing TP was exported downstream (12%). In comparison, only 5% of inflowing TOC was buried in sediments or removed via emission to the atmosphere in oxic conditions, resulting in 95% export downstream (Fig. 9). However, in some anoxic summers, the reservoir became a net source of TOC, DOC, and DRP downstream, meaning that inflowing TOC, DOC, and DRP - as well as TOC, DOC, and DRP that were previously retained in the reservoir sediments - were released and transported out of the reservoir (Fig. 8A,B,H). Consequently, on average, the reservoir exported 109% of inflowing TOC in anoxic conditions (Fig. 9).

The reservoir was a net source of TN, DIN, and NH_4^+ downstream even in oxic conditions, but this export significantly increased when the hypolimnion became anoxic in summer (Fig. 8C,D,E). The only fraction of N that did not exhibit higher downstream export during anoxic conditions was NO_3^- (Fig. 8F). During anoxic conditions, ~100% of inflowing NO_3^- was removed due to sediment denitrification, whereas in oxic conditions, some of this NO_3^- was exported downstream along with additional NO_3^- that originated from nitrified NH_4^+ in the reservoir (Fig. 7). Overall, the reservoir exported 195% of inflowing TN in summer oxic conditions and 602% in anoxic conditions (Fig. 9).

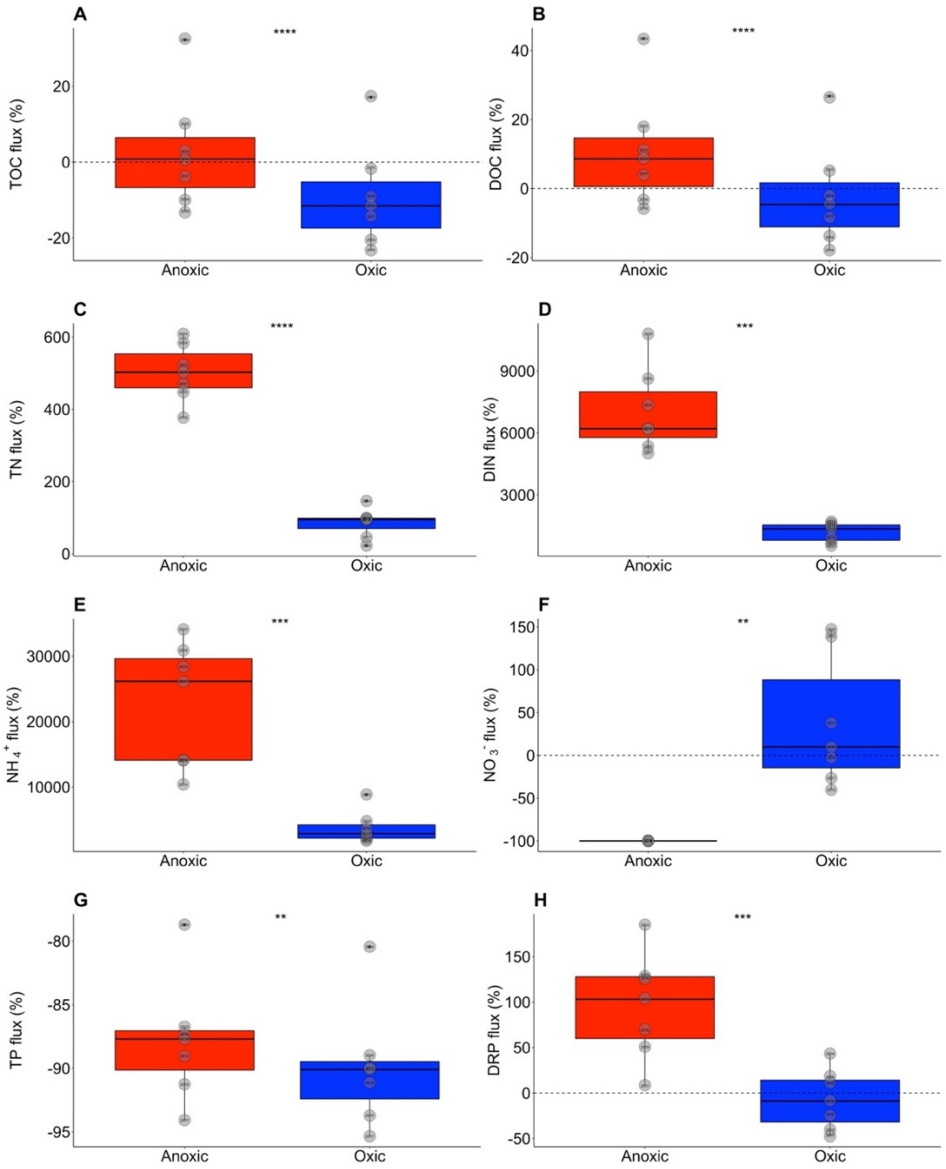

Fig. 8. Anoxia significantly increased the downstream export of total and dissolved fractions of organic carbon, nitrogen, and phosphorus. Percent downstream export (% flux) of total organic carbon (TOC; A), dissolved organic carbon (DOC; B), total nitrogen (TN; C), dissolved inorganic nitrogen (DIN; D), ammonium (NH_4^+; E), nitrate (NO_3^-; F), total phosphorus (TP; G), and dissolved reactive phosphorus (DRP; H) inputs into Falling Creek Reservoir for anoxic (red) and oxic (blue) model scenarios during the stratified period (July 15 - October 1) for all years of this study. Flux values of 0 (denoted by dashed horizontal lines) indicated that the reservoir inputs balanced exports; flux values <0 indicated that the reservoir was a net sink of C, N, or P; and flux values >0 indicated that the reservoir was a net source of C, N, or P downstream. The grey points are the median values from each of the seven years. The asterisks denote the p-values from paired t-tests comparing the median summer retention in anoxic and oxic scenarios: **** $p < 0.0001$, *** $p < 0.001$, and ** $p < 0.01$ (see Supplementary Text 5 for statistics). Note varying y-axes among panels.

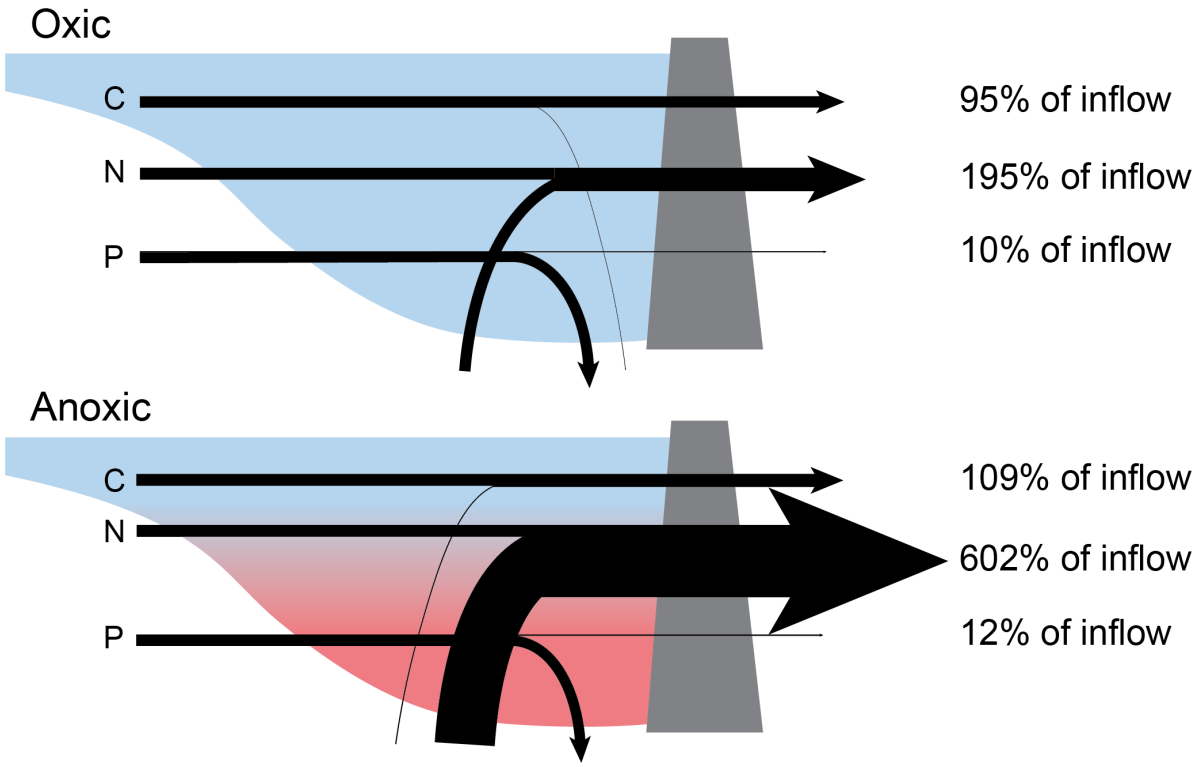

Fig. 9. Median summer downstream export of total organic carbon (C), total nitrogen (N), and total phosphorus (P) under oxic (top) and anoxic (bottom) conditions. The "percent of inflow" value represents the percent of inflowing C, N, and P into the reservoir that is exported downstream. A value of 100% indicates that reservoir inputs balanced exports; values <100% indicated that the reservoir was a net sink of C, N, or P; and values >100% indicated that the reservoir was a net source of C, N, or P downstream. Arrow widths are scaled to be proportional to the median downstream export of each element.

Despite low retention of inflowing TOC overall, FCR served as a net sink of POC in its sediments under both oxic and anoxic conditions. Across the seven years, FCR had marginally higher annual POC burial rates in anoxic (10.6 ± 1.1 g m^{-2} yr^{-1}) vs. oxic (mean 10.4 ± 1.1 g m^{-2} yr^{-1}) scenarios (p=0.10; Supplemental Text 5). The reservoir also served as a net sink of PON and POP, with significantly greater sediment burial of PON, but not POP, in anoxic scenarios than oxic scenarios (Supplementary Text 5).

Discussion

Our study provides one of the first comprehensive analyses on the effects of oxygen on multiple fractions of C, N, and P at the whole-ecosystem scale in a freshwater ecosystem. Our unprecedented 7-year field manipulation coupled with ecosystem model simulations reveals that anoxia may decrease the ability of reservoirs to serve as sinks of C, N, and P. Moreover, anoxia resulted in significantly higher summer concentrations of hypolimnetic NH_4^+, DRP, and DOC and altered dissolved and total stoichiometry by factors of 2-6×. Our integrated field manipulation and modeling study provides important insight on the biogeochemical cycling of these three elements, which are already changing in many freshwaters globally due to human activities (Powers et al. 2015, Maranger et al. 2018), and likely will change substantially more in the future as the prevalence and duration of anoxia in lakes and reservoirs increase (Tranvik et al. 2009, North et al. 2014, Jenny et al. 2016a, Jane et al. 2021). Below, we first examine the effects of anoxia on each elemental cycle separately, then their combined stoichiometry, and ultimately whole-ecosystem biogeochemical processing and fate.

554 *Hypolimnetic carbon and nutrient chemistry*

555 This study provides an answer to the critical question of how increased anoxia will affect
556 OC cycling at the whole-ecosystem scale (Sobek et al. 2009, Brothers et al. 2014, Peter et al.
557 2016, Mendonça et al. 2017, Carey et al. 2018). The shift in reservoir OC cycling in response to
558 anoxia is the consequence of changes in three linked processes: POC burial, DOC
559 mineralization, and DOC release from the sediments. Under anoxic conditions, POC burial
560 increased slightly, DOC mineralization rates were low, and DOC release from the sediments to
561 the water column was 2× higher than in oxic conditions (Fig. 7). Under oxic conditions, DOC
562 mineralization rates, while higher than in anoxic conditions (Fig. 7), were still an order of
563 magnitude lower than the rate of hydrologic flushing. The net outcome of these three processes
564 was a substantial difference in OC retention in the reservoir during oxic vs. anoxic conditions.
565 Under oxic conditions, the reservoir served as a net sink of DOC and TOC, with up to 18% of
566 inflowing DOC and 23% of inflowing TOC retained in a summer (Fig. 8A,B). Under anoxic
567 conditions, the decrease in net retention of inflowing DOC and TOC more than offset the slight
568 increase in POC burial, and nearly all of the inflowing DOC and TOC was exported downstream
569 (as indicated by 0% or positive flux in Fig. 8A,B). In five of the seven years, FCR even became a
570 net exporter of DOC in the anoxic scenario (Fig. 8B), meaning that both inflowing DOC and
571 likely legacy DOC that was previously buried in sediments were released and transported out of
572 the reservoir.

573 The finding that anoxia simultaneously increased the reservoir's role as a POC sink while
574 decreased its role as a DOC sink may explain some of the conflicting results that emerged from
575 previous studies that focused on only one OC fraction. First, our study supports past work that
576 observed increasing hypolimnetic DOC concentrations in anoxic conditions, suggesting that

anoxia decreases the freshwater OC sink (Brothers et al. 2014, Peter et al. 2016, Mendonça et al. 2017). The increasing hypolimnetic DOC concentrations have been attributed to both reductive dissolution of iron-bound OC complexes in the sediments during anoxia (Skoog and Arias-Esquivel 2009, Peter et al. 2016, Peter et al. 2017) and decreased mineralization rates in anoxic conditions (Bastviken et al. 2004, Sobek et al. 2009). Our calibrated ecosystem model indicates that both processes are important, but that the much higher hypolimnetic DOC concentrations in anoxic conditions in FCR were primarily due to sediment release (Fig. 7).

At the same time, our work also supports laboratory microcosm and sediment core studies that observed lower POC mineralization rates in anoxic than in oxic conditions (Bastviken et al. 2004, Sobek et al. 2009), leading to the expectation of greater POC burial in the sediments during anoxia. In FCR, mean summer POC hydrolysis rates in the hypolimnion were five orders of magnitude lower in anoxic than oxic conditions (Fig. 7), enabling slightly greater POC burial in anoxic than oxic conditions. Interestingly, a previous mass balance OC model calculated that POC burial in FCR during anoxic summer periods was ~12 g m^{-2} yr^{-1} (Carey et al. 2018), very similar to the 10.5 g m^{-2} yr^{-1} calculated with the numerical simulation model in this study. The overall similarity in burial rates across the two studies both validates our approach and confirms FCR's role as a small net POC sink, despite being a much a larger DOC source downstream under anoxic conditions. Altogether, our work indicates that using an ecosystem model to simultaneously track both concentrations and rates of the major processes affecting dissolved, particulate, and total pools of OC is needed to understand the full effects of oxygen on OC cycling, as different fractions have different responses to anoxia.

Nitrogen was the most sensitive of the three focal elements to anoxia, with an NH_4^+-dominated TN budget that increased dramatically during anoxic conditions. The dominant

mechanism driving the NH_4^+ increase in anoxic conditions were the approximately 4× higher rates of ammonification and sediment release than in oxic conditions (Fig. 7). Anammox and nitrification rates were very low in anoxic conditions (Fig. 7), enabling NH_4^+ to accumulate in the hypolimnion during anoxia. In oxic conditions, nitrification rates were unable to balance sediment fluxes, resulting in much lower but still noticeable increases in summer NH_4^+ concentrations (Fig. 4G). As a result, the reservoir functioned as an NH_4^+ source downstream regardless of hypolimnetic oxygen availability, though anoxia increased downstream fluxes by 7× relative to oxic conditions, on average. The high sediment NH_4^+ fluxes - even in oxic conditions - indicate that FCR has a large sediment NH_4^+ pool, which is likely due to historical agriculture in the catchment (Gerling et al. 2016). Until agricultural abandonment in the 1930s, most of FCR's catchment was farmland (Gerling et al. 2016). Even though the catchment did not experience industrial farming, agriculture can have century-long effects on soil properties, erosion, and ecosystem functioning (Foster et al. 2003, Cusack et al. 2013), resulting in a large pool of NH_4^+ that can be recycled between the hypolimnion and sediments for many years before eventual export (Ahlgren et al. 1994, Gerling et al. 2016).

Following expectation, hypolimnetic NO_3^- concentrations were significantly higher in oxic conditions than anoxic conditions. Despite an increase in NO_3^- during oxic conditions, the dominance of NH_4^+ over NO_3^- in the DIN pool (due to high NH_4^+ sediment fluxes even in oxic conditions; Fig. 7) resulted in overall similar patterns for TN and NH_4^+ (Fig. 5C,D,E). We initially anticipated that an increase in NO_3^- in oxic conditions could balance an increase in NH_4^+ in anoxic conditions, thereby resulting in similar DIN concentrations regardless of oxygen level, but low nitrification rates prevented increases in NO_3^- from occurring in oxic conditions (Fig. 7). Long-term water chemistry monitoring of FCR shows much lower summer NO_3^- concentrations

623 over time relative to NH_4^+ (Fig. 3E,F), and thus modeled results follow observations. In the
624 anoxic scenario, denitrification rates at the sediments were higher than in the water column,
625 whereas in the oxic scenario, denitrification rates in the water column were higher than at the
626 sediments (Fig. 7), as also observed in Swiss lakes with varying oxygen levels (Müller et al.
627 2021).

628 Altogether, anoxia significantly decreased FCR's role as a NH_4^+ sink while increased its
629 role as an NO_3^- sink (Fig. 8E,F) to the extent that ~100% of inflowing NO_3^- was removed via
630 denitrification. A previous study reported an average TN retention rate of 26% (and up to 78%)
631 of inputs for agricultural reservoirs in the U.S. (Powers et al. 2015). It would be expected that
632 FCR, which is located in a forested catchment, to have much higher TN retention than
633 agricultural reservoirs because of its lower external TN loads, however, FCR's high export of
634 NH_4^+ resulted in the reservoir serving as a source of TN downstream regardless of hypolimnetic
635 oxygen availability (Fig. 9). We anticipate that a greater duration and prevalence of hypolimnetic
636 anoxia in lakes and reservoirs could increase freshwater NO_3^- retention, while decreasing TN
637 retention if a waterbody's DIN pool is dominated by NH_4^+, as in FCR.

638 Summer hypolimnetic DRP concentrations were approximately 2× higher in anoxic
639 conditions than oxic conditions (Fig. 5H). DRP cycling was primarily controlled by sediment
640 fluxes (Fig. 7), which encompassed both release from metal complexes and sediment organic
641 matter into the water column. Our observation of 2× higher sediment release rates of DRP in
642 anoxic than oxic conditions (Fig. 7) follows decades of work that have observed similar patterns
643 of increased P fluxes during anoxia (Nürnberg 1987, Boström et al. 1988, Rydin 2000,
644 Søndergaard et al. 2003). The novelty of our study is that we simultaneously quantified both
645 dissolved and total pools of P at the whole-ecosystem scale in our model, allowing us to

disentangle the responses of different P fractions to anoxia. While DRP concentrations doubled in response to anoxia, TP concentrations only slightly increased (Fig. 4I,J), indicating an overall insensitivity of particulate P to hypolimnetic oxygen conditions in FCR. We did observe a small increase in dissolved organic P mineralization rates in response to higher oxygen (Fig. 7), but overall the particulate P burial rate in FCR did not vary between anoxic and oxic scenarios (Supplementary Text 5). Consequently, we expect that the P sink in reservoirs will be more resilient to anoxia than the C and N sinks, especially if the hypolimnetic DRP pool only comprises a small proportion of the TP pool, as observed in FCR (median of 11±1%).

Shifts in stoichiometry in response to anoxia

The substantial difference in stoichiometric ratios between anoxic and oxic conditions has important implications for understanding how anoxia affects the ecosystem functioning of lakes and reservoirs. Because anoxia increased hypolimnetic NH_4^+ concentrations more than any other dissolved or total fraction in this study, and NH_4^+ dominated both the dissolved and total N pools, any stoichiometric ratios that included NH_4^+, DIN, or TN exhibited large shifts during anoxia (Fig. 6). The significantly higher TN:TP and DIN:DRP ratios observed during anoxia will likely affect water quality and food web structure (Fig. 6G,H). Higher N:P ratios favor non-N-fixing cyanobacteria and will shift the composition of other taxa in phytoplankton community based on their N and P requirements (Reynolds 2006), as phytoplankton can access hypolimnetic nutrients via multiple mechanisms (Cottingham et al. 2015). In contrast, the significantly lower TOC:TN, DOC:DIN, and DOC:NH_4^+ ratios during anoxia could increase organic matter mineralization rates in the reservoir, as demonstrated in streams by Coble et al. (2015) (Fig. 6A,C,D). While DOC:DRP ratios significantly decreased in response to anoxia, TOC:TP ratios

669 did not significantly change (Fig. 6B,F), which is likely because the particulate P pool dominated
670 the TP budget and was largely insensitive to the effects of oxygen.
671 Our results both support and contradict earlier studies that measured freshwater
672 stoichiometry across many waterbodies. Similar to an analysis of >27,000 freshwater samples
673 from U.S. waterbodies (Helton et al. 2015), we observed inverse relationships between NO_3^- vs.
674 NH_4^+ concentrations and DOC vs. DIN concentrations (Fig. 6). Our study provides experimental
675 evidence to support the hypothesis that redox gradients are a major driver of NO_3^-:NH_4^+ and
676 DOC:DIN ratios, which will increase in oxic conditions and decrease in anoxic conditions
677 (Helton et al. 2015). On the other hand, our work finds only partial support for earlier findings of
678 lower TOC:TP and TN:TP ratios in reservoirs than natural lakes in an analysis of ~1000 U.S.
679 waterbodies, which was attributed in part to a greater incidence of anoxia in reservoirs
680 (Maranger et al. 2018). Median TOC:TP and TN:TP ratios in the reservoirs of that study were
681 417 and 38, respectively, which are similar to the ratios observed in FCR (Fig. 6B,G). However,
682 we did not see a significant difference in TOC:TP between anoxic and oxic scenarios (Fig. 6B),
683 suggesting that the differences in TOC:TP between reservoirs and natural lakes are likely not due
684 to anoxia. Moreover, we observed a significantly higher TN:TP ratio in anoxic conditions
685 relative to oxic conditions (Fig. 6G), indicating that individual waterbodies' responses to anoxia
686 may be dependent on the dominance of NO_3^- vs. NH_4^+ in their DIN pool prior to the onset of
687 anoxia: if NO_3^- dominates, then TN:TP ratios will likely decrease with anoxia, while if NH_4^+
688 dominates, then TN:TP ratios will likely increase. In general, most lakes tend to have higher
689 NO_3^- than NH_4^+ concentrations (Quirós 2003, Leoni et al. 2018), suggesting that anoxia may
690 result in lower TN:TP ratios in most waterbodies.
691

Opportunities and challenges of our whole-ecosystem approach

Our coupled field manipulation and modeling study provided a powerful approach for quantifying freshwater ecosystem responses to anoxia. Ideally, we would have run the REDOX field manipulation with multiple summers of continuous oxygenation and multiple summers of no oxygenation to contrast hypolimnetic conditions. However, we were constrained in our manipulation as the reservoir was an active drinking water source during the study, necessitating us to activate the oxygenation system every summer for the preservation of water quality. Consequently, we used the calibrated ecosystem model to simulate the biogeochemistry of continuously-oxygenated and never-oxygenated scenarios, which uniquely enabled us to compare the effect of oxygenation while holding all other factors constant, such as temperature (Fig. 4A).

The simulation model provided insights to reservoir responses to anoxia that would have been challenging to glean from field observations alone. We used the model to calculate whole-ecosystem rates that are impossible to measure in the field (e.g., daily POC burial), determine the relative importance of different processes for biogeochemical budgets, and quantify how processes changed in anoxic vs. oxic conditions. While the model's biogeochemical rates were determined from automated optimization and calibration of numerical simulation parameters, they fall within reasonable ranges of biogeochemical rates observed in the field, supporting our model results. For example, hypolimnetic sediment flux chamber measurements that were made in FCR in summer 2018 measured a mean sediment oxygen demand of ~20 mmol m^{-2} d^{-1} (range 8-37.5 mmol m^{-2} d^{-1}), which compares well with our calibrated hypolimnetic flux of 29 mmol m^{-2} d^{-1} (Krueger et al. 2020). That study also measured NH_4^+, DRP, and DOC fluxes from the sediment into the water column as the chambers became anoxic, which calculated release rates

up to 2.7 mmol NH_4^+ m^{-2} d^{-1}, 0.01 mmol DRP m^{-2} d^{-1}, and 14 mmol DOC m^{-2} d^{-1} (Supplementary Text 1). These numbers are consistent with our maximum calibrated rates of 2.8 mmol NH_4^+ m^{-2} d^{-1} and 0.01 mmol DRP m^{-2} d^{-1} (Carey et al. 2021c). Our maximum calibrated rate for DOC sediment flux, 1.4 mmol DOC m^{-2} d^{-1}, is an order of magnitude lower than the field data, suggesting that our modeled sediment flux rate of DOC was likely conservative.

We note several limitations to our study that should be considered. First, we focused on the hypolimnion of FCR as a reactor in which we could isolate coupled biogeochemical processes occurring during summer stratification, when C, N, and P processing rates are usually at their highest due to warm temperatures. This focus on the hypolimnion precluded other important processes that can have large effects on biogeochemical cycling in the epilimnion (e.g., photodegradation). Second, the ecosystem model is inherently limited in that it does not include all processes that can affect C, N, and P cycling (e.g., microbial dynamics, bioturbation). Third, similar to many other lake modeling studies (e.g., Kara et al. 2012, Farrell et al. 2020, Ward et al. 2020), it was challenging to model TP and DRP. For these two solutes in particular, most of the variation in observations was within the limit of quantitation (Supplementary Text 2), indicating that the model should not necessarily be penalized for the low performance in its evaluation metrics. Despite these challenges, the P parameters used for modeling FCR are consistent with other applications of the GLM-AED for other lakes (Kara et al. 2012, Farrell et al. 2020, Ward et al. 2020), and overall we were generally able to recreate observed physical, chemical, and biological dynamics in both the epilimnion and hypolimnion (Fig. 3, Supplementary Text 4).

Conclusions

The duration, prevalence, and magnitude of anoxia in the bottom waters of lakes and reservoirs are increasing globally (Butcher et al. 2015, Jenny et al. 2016a, Jane et al. 2021). While low oxygen conditions are typically thought of as a response to land use and climate change (Jenny et al. 2016b, Jane et al. 2021), our analysis demonstrates that low oxygen is itself a *driver* of major changes to freshwater biogeochemical cycling. Importantly, our work indicates that anoxia may alter the ability of lakes and reservoirs to serve as sinks of C, N, and P in the landscape. Consequently, while hypolimnetic anoxia is a result of increased C, N, and P loading into a waterbody, we also show that it may serve as an intensifying feedback that increases anoxia in downstream waterbodies. This is evident in our study, as we found significantly higher fluxes of C, N, and P downstream when FCR was exhibiting anoxic vs. oxic conditions during the summer. While more data are needed to evaluate the consequences of this feedback on downstream water quality, we hypothesize that it could be an important process affecting water quality in some freshwater ecosystems. Given the vital role that inland waters play in removing C, N, and P from downstream export (Harrison et al. 2009, Powers et al. 2016, Maranger et al. 2018), an increased prevalence and duration of anoxia in lakes and reservoirs will likely have major effects on global C, N, and P budgets as well as water quality and ecosystem functioning.

Acknowledgments

We thank the Western Virginia Water Authority, especially Jamie Morris, for their long-term partnership and support. We thank Paul Gantzer, John Little, Jonathan Doubek, Kathryn Krueger, and François Birgand for assistance with REDOX, and many field and lab assistants past and present in the Reservoir Group. This work was financially supported by the National

761 Science Foundation (DEB-1753639, DEB-1753657, CNS-1737424, DBI-1933016, DGE-
762 1651272), Fralin Life Sciences Institute, Institute for Critical Technology and Applied Science,
763 and Virginia Tech Global Change Center.

764

765 **References**

766 Ahlgren, I., T. Waara, K. Vrede, and F. Soerensson. 1994. Nitrogen budgets in relation to
767 microbial transformations in lakes. Ambio **23**:367-377.
768 APHA. 2017. Standard Methods for the Examination of Water and Wastewater, 23rd Ed.
769 American Public Health Association, American Water Works Association, Washington
770 DC.
771 Bastviken, D., J. Cole, M. Pace, and L. Tranvik. 2004. Methane emissions from lakes:
772 Dependence of lake characteristics, two regional assessments, and a global estimate.
773 Global Biogeochemical Cycles **18**:GB4009.
774 Beaulieu, J. J., R. L. Smolenski, C. T. Nietch, A. Townsend-Small, M. S. Elovitz, and J. P.
775 Schubauer-Berigan. 2014. Denitrification alternates between a source and sink of nitrous
776 oxide in the hypolimnion of a thermally stratified reservoir. Limnology and
777 Oceanography **59**:495-506.
778 Beusen, A. H. W., A. F. Bouwman, L. P. H. Van Beek, J. M. Mogollón, and J. J. Middelburg.
779 2016. Global riverine N and P transport to ocean increased during the 20th century
780 despite increased retention along the aquatic continuum. Biogeosciences **13**:2441-2451.
781 Beutel, M., N. Burley, and K. Culmer. 2006. Quantifying the effects of water velocity and
782 oxygen on sediment oxygen demand. Hydrological Sciences & Technology **22**:271-228.

783 Beutel, M. W. 2003. Hypolimnetic anoxia and sediment oxygen demand in California drinking
784 water reservoirs. Lake and Reservoir Management **19**:208-221.
785 Boström, B., J. M. Andersen, S. Fleischer, and M. Jansson. 1988. Exchange of phosphorus
786 across the sediment-water interface. Hydrobiologia **170**:229-244.
787 Brothers, S., J. Köhler, K. Attermeyer, H. P. Grossart, T. Mehner, N. Meyer, K. Scharnweber,
788 and S. Hilt. 2014. A feedback loop links brownification and anoxia in a temperate,
789 shallow lake. Limnology and Oceanography **59**:1388-1398.
790 Bruce, L., M. Frassl, G. Arhonditsis, G. Gal, D. Hamilton, P. Hanson, A. Hetherington, J.
791 Melack, J. Read, K. Rinke, A. Rigosi, D. Trolle, L. Winslow, R. Adrian, A. Ayala
792 Zamora, S. Bocaniov, B. Boehrer, C. Boon, J. Brookes, and M. Hipsey. 2018. A multi-
793 lake comparative analysis of the General Lake Model (GLM): Stress-testing across a
794 global observatory network. Environmental Modelling and Software **102**:274-291.
795 Butcher, J. B., D. Nover, T. E. Johnson, and C. M. Clark. 2015. Sensitivity of lake thermal and
796 mixing dynamics to climate change. Climatic Change **129**:295-305.
797 Carey, C. C., J. P. Doubek, R. P. McClure, and P. C. Hanson. 2018. Oxygen dynamics control
798 the burial of organic carbon in a eutrophic reservoir. Limnology and Oceanography
799 Letters **3**:293-301.
800 Carey, C. C., J. P. Doubek, J. H. Wynne, and B. R. Niederlehner. 2020. Dissolved silica time
801 series for Beaverdam Reservoir, Carvins Cove Reservoir, Claytor Lake, Falling Creek
802 Reservoir, Gatewood Reservoir, Smith Mountain Lake, and Spring Hollow Reservoir in
803 southwestern Virginia, USA during 2014, ver 1. Environmental Data Initiative
804 Repository. https://doi.org/10.6073/pasta/353aa34bedfd68800c12275633811341

Carey, C. C., A. G. Hounshell, M. E. Lofton, B. Birgand, B. J. Bookout, R. S. Corrigan, A. B. Gerling, R. P. McClure, and W. M. Woelmer. 2021a. Discharge time series for the primary inflow tributary entering Falling Creek Reservoir, Vinton, Virginia, USA 2013-2021, ver 7. Environmental Data Initiative repository. https://doi.org/10.6073/pasta/8d22a432aac5560b0f45aa1b21ae4746

Carey, C. C., A. S. Lewis, R. P. McClure, A. B. Gerling, S. Chen, A. Das, J. P. Doubek, D. W. Howard, M. E. Lofton, K. D. Hamre, and H. L. Wander. 2021b. Time series of high-frequency profiles of depth, temperature, dissolved oxygen, conductivity, specific conductivity, chlorophyll a, turbidity, pH, oxidation-reduction potential, photosynthetic active radiation, and descent rate for Beaverdam Reservoir, Carvins Cove Reservoir, Falling Creek Reservoir, Gatewood Reservoir, and Spring Hollow Reservoir in Southwestern Virginia, USA 2013-2020, ver 11. Environmental Data Initiative repository. https://doi.org/10.6073/pasta/5448f9d415fd09e0090a46b9d4020ccc

Carey, C. C., R. Q. Thomas, and P. C. Hanson. 2021c. General Lake Model-Aquatic EcoDynamics model parameter set for Falling Creek Reservoir, Vinton, Virginia, USA 2013-2019, ver 2. Environmental Data Initiative repository, https://portal-s.edirepository.org/nis/mapbrowse?packageid=edi.471.2.

Carey, C. C., R. Q. Thomas, R. P. McClure, A. G. Hounshell, W. M. Woelmer, H. L. Wander, and A. S. L. Lewis. 2021d. CareyLabVT/FCR-GLM: FCR GLM-AED model, data, and code for Carey et al. manuscript (v1.0). Zenodo, https://doi.org/10.5281/zenodo.5528865.

Carey, C. C., H. L. Wander, W. M. Woelmer, M. E. Lofton, A. Breef-Pilz, J. P. Doubek, A. B. Gerling, A. G. Hounshell, R. P. McClure, and B. R. Niederlehner. 2021e. Water chemistry time series for Beaverdam Reservoir, Carvins Cove Reservoir, Falling Creek

828 Reservoir, Gatewood Reservoir, and Spring Hollow Reservoir in southwestern Virginia,
829 USA 2013-2020, ver 8. Environmental Data Initiative repository.
830 https://doi.org/10.6073/pasta/8d83ef7ec202eca9192e3da6dd34a4e0
831 Carey, C. C., W. M. Woelmer, J. T. Maze, and A. G. Hounshell. 2019. Manually-collected
832 discharge data for multiple inflow tributaries entering Falling Creek Reservoir and
833 Beaverdam Reservoir, Vinton, Virginia, USA in 2019, ver 4. Environmental Data
834 Initiative repository. https://doi.org/10.6073/pasta/4d8e7b7bedbc6507b307ba2d5f2cf9a2
835 Carey, C. C., J. H. Wynne, H. L. Wander, R. P. McClure, K. J. Farrell, A. Breef-Pilz, J. P.
836 Doubek, A. B. Gerling, K. D. Hamre, A. G. Hounshell, A. S. Lewis, M. E. Lofton, and
837 W. M. Woelmer. 2021f. Secchi depth data and discrete depth profiles of
838 photosynthetically active radiation, temperature, dissolved oxygen, and pH for
839 Beaverdam Reservoir, Carvins Cove Reservoir, Falling Creek Reservoir, Gatewood
840 Reservoir, and Spring Hollow Reservoir in southwestern Virginia, USA 2013-2020, ver
841 8. Environmental Data Initiative repository.
842 https://doi.org/10.6073/pasta/3e9f27971e353c8a80840b5e99a67d0c
843 Coble, A., A. Marcarelli, and E. Kane. 2015. Ammonium and glucose amendments stimulate
844 dissolved organic matter mineralization in a Lake Superior tributary. Journal of Great
845 Lakes Research **41**:801-807.
846 Cottingham, K. L., H. A. Ewing, M. L. Greer, C. C. Carey, and K. C. Weathers. 2015.
847 Cyanobacteria as biological drivers of lake nitrogen and phosphorus cycling. Ecosphere
848 **6**:art1. DOI: 10.1890/ES14-00174.1

849 Cusack, D. F., O. A. Chadwick, T. Ladefoged, and P. M. Vitousek. 2013. Long-term effects of
850 agriculture on soil carbon pools and carbon chemistry along a Hawaiian environmental
851 gradient. Biogeochemistry **112**:229-243.
852 Downes, M. T. 1987. Aquatic nitrogen transformations at low oxygen concentrations. Applied
853 and Environmental Microbiology **54**:172-175.
854 Downing, J. A., Y. T. Prairie, J. J. Cole, C. M. Duarte, L. J. Tranvik, R. G. Striegl, W. H.
855 McDowell, P. Kortelainen, N. F. Caraco, J. M. Melack, and J. J. Middelburg. 2006. The
856 global abundance and size distribution of lakes, ponds, and impoundments. Limnology
857 and Oceanography **51**:2388-2397.
858 Farrell, K. J., N. K. Ward, A. I. Krinos, P. C. Hanson, V. Daneshmand, R. J. Figueiredo, and C.
859 C. Carey. 2020. Ecosystem-scale nutrient cycling responses to increasing air
860 temperatures vary with lake trophic state. Ecological Modelling **430**:109134.
861 Foster, D., F. Swanson, J. Aber, I. Burke, N. Brokaw, D. Tilman, and A. Knapp. 2003. The
862 importance of land-use legacies to ecology and conservation. Bioscience **53**:77-88.
863 Frindte, K., M. Allgaier, H.-P. Grossart, and W. Eckert. 2015. Microbial response to
864 experimentally controlled redox transitions at the sediment water interface. PLoS One
865 **10**:e0143428.
866 Gerling, A., R. Browne, P. Gantzer, M. Mobley, J. Little, and C. Carey. 2014. First report of the
867 successful operation of a side stream supersaturation hypolimnetic oxygenation system in
868 a eutrophic, shallow reservoir. Water Research **67**:129-143.
869 Gerling, A. B., Z. W. Munger, J. P. Doubek, K. D. Hamre, P. A. Gantzer, J. C. Little, and C. C.
870 Carey. 2016. Whole-catchment manipulations of internal and external loading reveal the
871 sensitivity of a century-old reservoir to hypoxia. Ecosystems **19**:555-571.

872 Hansen, N. 2016. The CMA evolution strategy: A tutorial. ArXiv **160400772**.
873 https://arxiv.org/abs/1604.00772
874 Hanson, P. C., M. L. Pace, S. R. Carpenter, J. J. Cole, and E. H. Stanley. 2015. Integrating
875 landscape carbon cycling: research needs for resolving organic carbon budgets of lakes.
876 Ecosystems **18**:363-375.
877 Harrison, J. A., R. J. Maranger, R. B. Alexander, A. E. Giblin, P.-A. Jacinthe, E. Mayorga, S. P.
878 Seitzinger, D. J. Sobota, and W. M. Wollheim. 2009. The regional and global
879 significance of nitrogen removal in lakes and reservoirs. Biogeochemistry **93**:143-157.
880 Helton, A. M., M. Ardón, and E. S. Bernhardt. 2015. Thermodynamic constraints on the utility
881 of ecological stoichiometry for explaining global biogeochemical patterns. Ecology
882 Letters **18**:1049-1056.
883 Hipsey, M. R., L. C. Bruce, C. Boon, B. Busch, C. C. Carey, D. P. Hamilton, P. C. Hanson, J. S.
884 Read, E. de Sousa, M. Weber, and L. A. Winslow. 2019. A General Lake Model (GLM
885 3.0) for linking with high-frequency sensor data from the Global Lake Ecological
886 Observatory Network (GLEON). Geoscience Model Development **12**:473-523.
887 Jane, S. F., G. J. A. Hansen, B. M. Kraemer, P. R. Leavitt, J. L. Mincer, R. L. North, R. M. Pilla,
888 J. T. Stetler, C. E. Williamson, R. I. Woolway, L. Arvola, S. Chandra, C. L. DeGasperi,
889 L. Diemer, J. Dunalska, O. Erina, G. Flaim, H.-P. Grossart, K. D. Hambright, C. Hein, J.
890 Hejzlar, L. L. Janus, J.-P. Jenny, J. R. Jones, L. B. Knoll, B. Leoni, E. Mackay, S.-I. S.
891 Matsuzaki, C. McBride, D. C. Müller-Navarra, A. M. Paterson, D. Pierson, M. Rogora, J.
892 A. Rusak, S. Sadro, E. Saulnier-Talbot, M. Schmid, R. Sommaruga, W. Thiery, P.
893 Verburg, K. C. Weathers, G. A. Weyhenmeyer, K. Yokota, and K. C. Rose. 2021.
894 Widespread deoxygenation of temperate lakes. Nature **594**:66-70.

895 Jenny, J.-P., P. Francus, A. Normandeau, F. Lapointe, M.-E. Perga, A. Ojala, A. Schimmelmann,
896 and B. Zolitschka. 2016a. Global spread of hypoxia in freshwater ecosystems during the
897 last three centuries is caused by rising local human pressure. Global Change Biology
898 **22**:1481-1489.
899 Jenny, J.-P., A. Normandeau, P. Francus, Z. E. Taranu, I. Gregory-Eaves, F. Lapointe, J. Jautzy,
900 A. E. K. Ojala, J.-M. Dorioz, A. Schimmelmann, and B. Zolitschka. 2016b. Urban point
901 sources of nutrients were the leading cause for the historical spread of hypoxia across
902 European lakes. Proceedings of the National Academy of Sciences **113**:12655.
903 Kara, E. L., P. Hanson, D. Hamilton, M. R. Hipsey, K. D. McMahon, J. S. Read, L. Winslow, J.
904 Dedrick, K. Rose, C. C. Carey, S. Bertilsson, D. da Motta Marques, L. Beversdorf, T.
905 Miller, C. Wu, Y.-F. Hsieh, E. Gaiser, and T. Kratz. 2012. Time-scale dependence in
906 numerical simulations: Assessment of physical, chemical, and biological predictions in a
907 stratified lake at temporal scales of hours to months. Environmental Modelling &
908 Software **35**:104-121.
909 Kim, C., Y. Nishimura, and T. Nagata. 2006. Role of dissolved organic matter in hypolimnetic
910 mineralization of carbon and nitrogen in a large, monomictic lake. Limnology and
911 Oceanography **51**:70-78.
912 Krueger, K. M., C. E. Vavrus, M. E. Lofton, R. P. McClure, P. Gantzer, C. C. Carey, and M. E.
913 Schreiber. 2020. Iron and manganese fluxes across the sediment-water interface in a
914 drinking water reservoir. Water Research **182**:116003.
915 Ladwig, R., P. C. Hanson, H. A. Dugan, C. C. Carey, Y. Zhang, L. Shu, C. J. Duffy, and K. M.
916 Cobourn. 2021. Lake thermal structure drives interannual variability in summer anoxia

dynamics in a eutrophic lake over 37 years. Hydrology and Earth System Science **25**:1009-1032.

Lau, M. P., M. Sander, J. Gelbrecht, and M. Hupfer. 2016. Spatiotemporal redox dynamics in a freshwater lake sediment under alternating oxygen availabilities: combined analyses of dissolved and particulate electron acceptors. Environmental Chemistry **13**:826-837.

Lehner, B., C. R. Liermann, C. Revenga, C. Vörösmarty, B. Fekete, P. Crouzet, P. Döll, M. Endejan, K. Frenken, J. Magome, C. Nilsson, J. C. Robertson, R. Rödel, N. Sindorf, and D. Wisser. 2011. High-resolution mapping of the world's reservoirs and dams for sustainable river-flow management. Frontiers in Ecology and the Environment **9**:494-502.

Leoni, B., M. Patelli, V. Soler, and V. Nava. 2018. Ammonium transformation in 14 lakes along a trophic gradient. Water **10**. DOI: 10.3390/w10030265

Maranger, R., S. E. Jones, and J. B. Cotner. 2018. Stoichiometry of carbon, nitrogen, and phosphorus through the freshwater pipe. Limnology and Oceanography Letters **3**:89-101.

Medlyn, B. E., S. Zaehle, M. G. De Kauwe, A. P. Walker, M. C. Dietze, P. J. Hanson, T. Hickler, A. K. Jain, Y. Luo, W. Parton, I. C. Prentice, P. E. Thornton, S. Wang, Y.-P. Wang, E. Weng, C. M. Iversen, H. R. McCarthy, J. M. Warren, R. Oren, and R. J. Norby. 2015. Using ecosystem experiments to improve vegetation models. Nature Climate Change **5**:528-534.

Mendonça, R., R. A. Müller, D. Clow, C. Verpoorter, P. Raymond, L. J. Tranvik, and S. Sobek. 2017. Organic carbon burial in global lakes and reservoirs. Nature Communications **8**:1694.

939 Morris, M. D. 1991. Factorial sampling plans for preliminary computational experiments.
940 Technometrics **33**:161-174.
941 Müller, B., R. Thoma, K. B. L. Baumann, C. M. Callbeck, and C. J. Schubert. 2021. Nitrogen
942 removal processes in lakes of different trophic states from on-site measurements and
943 historic data. Aquatic Sciences **83**:art37.
944 North, R. P., R. L. North, D. M. Livingstone, O. Köster, and R. Kipfer. 2014. Long-term changes
945 in hypoxia and soluble reactive phosphorus in the hypolimnion of a large temperate lake:
946 consequences of a climate regime shift. Global Change Biology **20**:811-823.
947 Nürnberg, G. K. 1987. A comparison of internal phosphorus loads in lakes with anoxic
948 hypolimnia. Limnology and Oceanography **32**:1160-1164.
949 Nürnberg, G. K. 1988. Prediction of phosphorus release rates from total and reductant-soluble
950 phosphorus in anoxic lake sediments. Canadian Journal of Fisheries and Aquatic Sciences
951 **45**:453-462.
952 Peter, S., O. Agstam, and S. Sobek. 2017. Widespread release of dissolved organic carbon from
953 anoxic boreal lake sediments. Inland Waters **7**:151-163.
954 Peter, S., A. Isidorova, and S. Sobek. 2016. Enhanced carbon loss from anoxic lake sediment
955 through diffusion of dissolved organic carbon. Journal of Geophysical Research:
956 Biogeosciences **121**:1959-1977.
957 Powers, S. M., T. W. Bruulsema, T. P. Burt, N. I. Chan, J. J. Elser, P. M. Haygarth, N. J. K.
958 Howden, H. P. Jarvie, Y. Lyu, H. M. Peterson, Andrew N. Sharpley, J. Shen, F. Worrall,
959 and F. Zhang. 2016. Long-term accumulation and transport of anthropogenic phosphorus
960 in three river basins. Nature Geoscience **9**:353-356.

961 Powers, S. M., J. L. Tank, and D. M. Robertson. 2015. Control of nitrogen and phosphorus
962 transport by reservoirs in agricultural landscapes. Biogeochemistry **124**:417-439.
963 Quirós, R. 2003. The relationship between nitrate and ammonia concentrations in the pelagic
964 zone of lakes. Limnetica **22**:37-50.
965 Rydin, E. 2000. Potentially mobile phosphorus in Lake Erken sediment. Water Research
966 **34**:2037-2042.
967 Rysgaard, S., N. Risgaard-Petersen, N. Sloth, K. I. M. Jensen, and L. P. Nielsen. 1994. Oxygen
968 regulation of nitrification and denitrification in sediments. Limnology and Oceanography
969 **39**:1643-1652.
970 Sharma, B., and R. C. Ahlert. 1977. Nitrification and nitrogen removal. Water Research **11**:897-
971 925.
972 Skoog, A. C., and V. A. Arias-Esquivel. 2009. The effect of induced anoxia and reoxygenation
973 on benthic fluxes of organic carbon, phosphate, iron, and manganese. Science of the
974 Total Environment **407**:6085-6092.
975 Sobek, S., E. Durisch-Kaiser, R. Zurbrügg, N. Wongfun, M. Wessels, N. Pasche, and B. Wehrli.
976 2009. Organic carbon burial efficiency in lake sediments controlled by oxygen exposure
977 time and sediment source. Limnology and Oceanography **54**:2243-2254.
978 Søndergaard, M., J. P. Jensen, and E. Jeppesen. 2003. Role of sediment and internal loading of
979 phosphorus in shallow lakes. Hydrobiologia **506**:135-145.
980 Sterner, R., and J. J. Elser. 2002. Ecological Stoichiometry: The Biology of Elements From
981 Molecules to The Biosphere. Princeton University Press, Princeton, NJ.
982 R Core Team. 2020. R: A language and environment for statistical computing. Version 3.6.3. R
983 Foundation for Statistical Computing, Vienna, Austria.

984 Toming, K., J. Kotta, E. Uuemaa, S. Sobek, T. Kutser, and L. J. Tranvik. 2020. Predicting lake
985 dissolved organic carbon at a global scale. Scientific Reports **10**:8471.
986 Tranvik, L. J., J. A. Downing, J. B. Cotner, S. A. Loiselle, R. G. Striegl, T. J. Ballatore, P.
987 Dillon, K. Finlay, K. Fortino, L. B. Knoll, P. L. Kortelainen, T. Kutser, S. Larsen, I.
988 Laurion, D. M. Leech, S. L. McCallister, D. M. McKnight, J. M. Melack, E. Overholt, J.
989 A. Porter, Y. Prairie, W. H. Renwick, F. Roland, B. S. Sherman, D. W. Schindler, S.
990 Sobek, A. Tremblay, M. J. Vanni, A. M. Verschoor, E. von Wachenfeldt, and G. A.
991 Weyhenmeyer. 2009. Lakes and reservoirs as regulators of carbon cycling and climate.
992 Limnology and Oceanography **54**:2298-2314.
993 Verpoorter, C., T. Kutser, D. A. Seekell, and L. J. Tranvik. 2014. A global inventory of lakes
994 based on high-resolution satellite imagery. Geophysical Research Letters **41**:6396-6402.
995 Walker, R. R., and W. J. Snodgrass. 1986. Model for sediment oxygen demand in lakes. Journal
996 of Environmental Engineering **112**:25-43.
997 Ward, N. K., B. G. Steele, K. C. Weathers, K. L. Cottingham, H. A. Ewing, P. C. Hanson, and C.
998 C. Carey. 2020. Differential responses of maximum versus median chlorophyll-a to air
999 temperature and nutrient loads in an oligotrophic lake over 31 years. Water Resources
1000 Research **56**:e2020WR027296.
1001 Wetzel, R. G. 2001. Limnology: Lake and River Ecosystems. 3rd edition. Academic Press, New
1002 York.
1003 Woolway, R. I., S. Sharma, G. A. Weyhenmeyer, A. Debolskiy, M. Golub, D. Mercado-Bettín,
1004 M. Perroud, V. Stepanenko, Z. Tan, L. Grant, R. Ladwig, J. Mesman, T. N. Moore, T.
1005 Shatwell, I. Vanderkelen, J. A. Austin, C. L. DeGasperi, M. Dokulil, S. La Fuente, E. B.
1006 Mackay, S. G. Schladow, S. Watanabe, R. Marcé, D. C. Pierson, W. Thiery, and E.

1007 Jennings. 2021. Phenological shifts in lake stratification under climate change. Nature
1008 Communications **12**:2318.
1009 Xia, Y., K. Mitchell, M. Ek, J. Sheffield, B. Cosgrove, E. Wood, L. Luo, C. Alonge, H. Wei, J.
1010 Meng, B. Livneh, D. Lettenmaier, V. Koren, Q. Duan, K. Mo, Y. Fan, and D. Mocko.
1011 2012. Continental-scale water and energy flux analysis and validation for the North
1012 American Land Data Assimilation System project phase 2 (NLDAS-2): 1.
1013 Intercomparison and application of model products. Journal of Geophysical Research:
1014 Atmospheres **117**:D03109.
1015 Zarfl, C., A. E. Lumsdon, J. Berlekamp, L. Tydecks, and K. Tockner. 2015. A global boom in
1016 hydropower dam construction. Aquatic Sciences **77**:161-170.
1017

Supplementary Materials for

Anoxia decreases the magnitude of the carbon, nitrogen, and phosphorus sink in freshwaters

Cayelan C. Carey*, Paul C. Hanson, R. Quinn Thomas, Alexandra B. Gerling, Alexandria G. Hounshell, Abigail S. L. Lewis, Mary E. Lofton, Ryan P. McClure, Heather L. Wander, Whitney M. Woelmer, Barbara R. Niederlehner, Madeline E. Schreiber

*Corresponding author. Email: cayelan@vt.edu

This file includes:

Supplementary Text 1. Description of field monitoring methods at Falling Creek Reservoir.

Overview

Throughout the REDOX experiment in 2013-2019, Falling Creek Reservoir (FCR) was intensively monitored for water temperature, dissolved oxygen, chemistry, and phytoplankton (chlorophyll-a) concentrations for model calibration and validation. The two major inflows into FCR were also monitored for discharge, temperature, dissolved oxygen, and chemistry. The frequency of monitoring varied by time of year: during the spring (March-May), field sampling occurred weekly to fortnightly; from May-October, sampling occurred 1-2 times per week; and from November-March, sampling occurred approximately once every month or every other month. Monitoring occurred at the deepest lacustrine site in FCR next to the dam (see Fig. 2 in main text) as well as at the primary inflow stream to FCR (Tunnel Branch) from 2013-2019. In 2019, a second smaller inflow was also monitored (Falling Creek). All monitoring data are available with associated metadata in the Environmental Data Initiative repository (Carey et al. 2019, Carey et al. 2020, Carey et al. 2021a, Carey et al. 2021b, Carey et al. 2021f, Carey et al. 2021g), and described below.

Lacustrine monitoring

At the lacustrine sampling site, high-frequency (4 Hz) depth profiles of water temperature, dissolved oxygen, and chlorophyll-a were collected with a SeaBird Conductivity, Temperature, and Depth (CTD) profiler (Sea-Bird Scientific, Bellevue, WA, USA) on each sampling day from 2013-2019 (Carey et al. 2021b). On the few sampling days when the CTD was not available, we substituted a YSI handheld probe (ProPlus with Quattro cable or ProODO optical dissolved oxygen meter; YSI Inc., Yellow Springs, OH, USA) to measure depth profiles

of temperature and dissolved oxygen (Carey et al. 2021g). We collected paired CTD and YSI depth profiles on 60 days during 2015-2019, yielding n=674 observations throughout the water column for which we had replicate temperature and dissolved oxygen measurements. A comparison of the CTD and YSI data indicate that the methods were quantitatively similar (temperature Spearman's rho = 0.98, mean bias = 0.48^{o}C; dissolved oxygen rho = 0.82, mean bias = 0.44 mg L^{-1}).

We also collected water samples for total and dissolved nutrient (nitrogen and phosphorus) and organic carbon analysis from the reservoir's water treatment extraction depths (0.1, 1.6, 2.8, 3.8, 5.0, 6.2, 8.0, and 9.0 m) using a 4-L Van Dorn sampler (Wildco, Yulee, FL, USA). Water was filtered through GF/F (0.7 um) filters into acid-washed 125 mL HDPE bottles and immediately frozen for nitrate, ammonium, dissolved reactive phosphorus, and dissolved organic carbon analysis (Carey et al. 2021f). Unfiltered water was also frozen in separate acid-washed 125 mL HDPE bottles for total nitrogen and total phosphorus analysis (Carey et al. 2021f), as well as for total organic carbon analysis on a subset of sampling days in 2014 (Carey et al. 2018). In 2014, water samples were collected from 0.1, 5, and 9 m for dissolved reactive silica analysis (Carey et al. 2020). We focused our analysis on organic C, rather than inorganic C, because of the important role of reservoirs in burying this pool in the global C cycle (Mendonça et al. 2017), and because previous work indicates that most terrestrial dissolved inorganic C loads are rapidly emitted to the atmosphere (McDonald et al. 2013). All laboratory analysis methods are described in Supplementary Text 2.

Inflow monitoring

At Tunnel Branch, the primary inflow to FCR (Fig. 2 in main text), we measured

discharge and water temperature every 15 minutes using an INW Aquistar PT2X pressure sensor (INW, Kirkland, Washington, USA) throughout the study period. From 15 May 2013 to 6 June 2019, the weir was rectangular before it was converted to a V-notch weir on 7 June 2019. Rating curves and equations for calculating discharge, as well as data quality checks on the weir conversion, can be found in the metadata for the discharge dataset, available in the Environmental Data Initiative repository (Carey et al. 2021a). On each monitoring day from 2013-2019, we also collected water temperature and dissolved oxygen using a YSI handheld probe, as well as water samples for chemical analyses as described above.

Monitoring at Falling Creek, the second largest inflow to FCR, began in February 2019. Falling Creek did not have a weir, so we measured discharge at this inflow using a flowmeter (either a model FP 111 propeller flowmeter from Forestry Suppliers, Inc., Jackson, MS, USA or a model Flo-Mate 2000656 instantaneous velocity meter from Marsh-McBirney, Frederick, MD, USA). We used the flowmeter to measure velocity at 0.1-m increments along a transect across the inflow stream. These measurements were subsequently used to calculate discharge following (Gordon 2004). We periodically verified flowmeter measurements using both salt injection and velocity floats. Details regarding these ancillary measurements as well as all inflow discharge data are in the Environmental Data Initiative repository (Carey et al. 2019). We also collected water temperature and dissolved oxygen using the YSI probe as well as water samples for chemical analyses on each monitoring day at this inflow.

Sediment flux chambers

Benthic flux chambers were deployed in triplicate over the sediments in the hypolimnion of FCR during two 10-day experiments in summer 2018 (21 June – 2 July and 13 – 23 August)

to measure diffusive solute fluxes across the sediment-water interface (Krueger et al. 2020). The flux chambers isolated 64.86 L of hypolimnetic water and 0.27 m^2 of the hypolimnetic sediment surface. Each chamber contained an optical dissolved oxygen sensor (InsiteIG Model 31, Slidell, LA, USA) to measure temperature and dissolved oxygen. The sensors were connected to a data logger (Gantzer Water, Livingston, TX, USA), which collected data on 2-minute intervals.

During deployment, the chambers were slowly lowered from a boat through the water column to the bottom and were then flushed with hypolimnetic water for 90 – 120 minutes using a circulation pump until dissolved oxygen and temperature within the chamber stabilized. After deployment, the chambers were left undisturbed for 24 hours before water samples were collected from the chamber every 3 days for 10 days (Krueger et al. 2020). The chambers went anoxic typically within 2-3 days. During sampling, water within the chamber and tubing was slowly circulated for one minute before water samples were gently removed via tubing for dissolved organic carbon, ammonium, dissolved reactive phosphorus, dissolved iron, and dissolved manganese without disturbing the sediments (Krueger et al. 2020). Iron and manganese analytical methods and data are published in (Krueger et al. 2020). Dissolved organic carbon, ammonium, and dissolved reactive phosphorus analytical methods are described in Supplementary Text 2 and published in (Carey et al. 2021e).

The water chemistry samples were used to calculate sediment release rates for each solute into the hypolimnion. Fluxes were calculated using the equation:

$$J = b \times (V/A) \qquad \text{(eqn. S1)}$$

Where J is the flux of the solute (mmol m^{-2} d^{-1}), b is the slope of the best fit line of the solute concentrations plotted over time (mmol m^{-2} d^{-1}), V is the volume of the flux chamber (64.86 L), and A is the surface area of the flux chamber (0.27 m^2).

Supplementary Text 2. Laboratory water chemistry analysis detailed methods.

Overview and quality assurance/quality control procedures

Below, we describe the laboratory methods and quality control procedures we used to quantify carbon (dissolved organic carbon, total organic carbon), nitrogen (ammonia, nitrate, total nitrogen), phosphorus (dissolved reactive phosphorus and total phosphorus), and dissolved reactive silica in reservoir water samples.

For quality control and assurance of data, method detection limits, limits of quantitation, and long-term averages were calculated. Generally, method detection limits (MDL) were determined as a one-sided 99% confidence interval from repeated measurements of a low concentration standard (USEPA 1997). Limits of quantitation (LOQ) were calculated as 10 times the standard deviation (Currie 1968). These measures were calculated at least once each season. Long-term averages were calculated over all determinations within the study period and reported with a 95% confidence interval.

Values below the MDL were kept as reported by the instrument but flagged in the database as being below detection. Values below the LOQ were kept and not flagged. Negative values were set to zero and flagged in the database. If a sample was analyzed repeatedly and multiple valid measurements for an analyte were obtained, as might happen if a signal peak was improperly integrated for only one of several analytes reported by a particular instrument, the mean of the multiple valid measurements was calculated and reported. All chemical measurements used in the calibration and validation of the FCR GLM-AED model are published in the Environmental Data Initiative (EDI) repository (Carey et al. 2021f).

Carbon

Total and dissolved organic carbon concentrations were both determined by infrared absorbance after organic carbon was released from the samples as carbon dioxide by either heated persulfate digestion (APHA 2017e) or high temperature combustion (APHA 2017d). Long-term mean MDL and LOQ were 0.34 (0.11 to 0.56) and 1.13 (0.37 to 1.89) mg L^{-1}, respectively (calculated from n = 12 MDL determinations).

Nitrogen

Ammonia nitrogen (hereafter, ammonium) concentrations were determined colorimetrically using the phenate method on a Lachat QuikChem 8500 Flow Injection Analyzer (Lachat Instruments, Loveland, CO, USA) (Lachat 2007a, APHA 2017a). We adopted a common modification and used sodium dichloroisocyanuric acid as the source of hypochlorite ion because of its longer shelf life (following Grasshoff and Johannsen 1972, Zhang et al. 1997). Long-term mean MDL and LOQ were 2.9 (2.2-3.7) and 9.2 (7.0-11.3) µg L^{-1}, respectively (calculated from n = 32 MDL determinations).

Nitrate plus nitrite nitrogen (hereafter, nitrate) concentrations were determined colorimetrically using cadmium reduction followed by the Griess reaction on a Lachat QuikChem 8500 Flow Injection Analyzer (Lynch 2007, APHA 2017b). Long-term mean MDL and LOQ were 1.8 (1.4 to 2.2) and 5.7 (4.4 to 7.1) µg L^{-1}, respectively (calculated from n = 41 MDL determinations).

Total nitrogen concentrations were determined after an alkaline persulfate digestion (Patton and Kryskalla 2003) at sub-boiling temperatures (Doyle et al. 2004, Huang and Zhang 2009), followed by a colorimetric determination of the resulting nitrate using cadmium reduction

and the Griess reaction. The method was modified by the addition of 0.25 M sodium hydroxide to the sample before color development as described in (Egan 2013). Due to known contribution of reagents to nutrient burdens, concentrations were corrected by the mean of process blanks. Long-term mean MDL and LOQ were 14.2 (7.5 to 20.1) and 45.1 (23.8 to 66.5) µg L^{-1}, respectively (calculated from n = 53 MDL determinations).

Phosphorus

Dissolved reactive phosphorus concentrations were determined colorimetrically using the molybdenum blue method on a Lachat QuikChem 8500 Flow Injection Analyzer (Lachat 2007b, APHA 2017c). Long-term mean MDL and LOQ were 2.5 (2.0 to 3.0) and 7.6 (6.0 to 9.2) µg L^{-1}, respectively (calculated from n = 31 MDL determinations). For this analyte in particular, caution is warranted when interpreting potential differences in concentrations below the LOQ.

Total phosphorus concentrations were determined after an alkaline persulfate digestion (Patton and Kryskalla 2003) at sub-boiling temperatures (Zhang et al. 1997, Doyle et al. 2004), followed by a colorimetric determination of the resulting dissolved reactive phosphorus concentration using the molybdenum blue method. Due to known contribution of reagents to nutrient burdens, concentrations were corrected by the mean of process blanks. Long-term mean MDL and LOQ were 3.7 (2.9 to 4.5) and 11.7 (9.2 to 14.2) µg L^{-1}, respectively (calculated from n = 54 MDL determinations). As for total phosphorus, caution is warranted when interpreting potential differences in concentrations below the LOQ.

Silica

Dissolved reactive silica was determined colorimetrically using ammonium molybdate

184 followed by sodium sulfite reduction (Wetzel and Likens 2000) using a Shimadzu UV 1601
185 spectrophotometer (Shimadzu Corp., Kyoto, Japan). Dissolved reactive silica was only analyzed
186 for a subset of depths in 2014, and a limit of detection (LOD) and limit of quantitation (LOQ)
187 were estimated from the calibration curve (IUPAC 1997, Ranke 2018, Team 2020). The
188 estimated LOD was 0.39 mg L^{-1} and the estimated LOQ was 0.70 mg L^{-1}.
189
190 *Instrument overlap*
191 Some analytical instruments were replaced or updated during the 2013-2019 study
192 period. When transitioning between instruments, we conducted overlap studies (Table S1).
193 Correspondences in concentrations determined from the old vs. new instruments were assessed
194 with method comparison regression. We used Passing Bablock regression (Passing and Bablok
195 1983), a non-parametric form of error-in-variables regression. Estimates of slope and intercept
196 were determined and confidence intervals for the regression coefficients were quantified by
197 bootstrapping (Manuilova and Schuetzenmeister 2014). Good correspondence yields a slope near
198 1 and an intercept near 0, and a 95% confidence interval that does not include these best-case
199 values indicates a statistically-significant difference. If an intercept was significantly different
200 from 0, we compared the magnitude of this difference to the MDL. If the difference was within 2
201 of the MDL, the correspondence was judged to be acceptable for inclusion of both old and new
202 instrument concentrations in subsequent data analyses. If a slope was significantly different from
203 1, we evaluated both the magnitude of the difference and plots of residuals vs. concentrations. If
204 there was no clear pattern over increasing concentration, the correspondence was judged
205 acceptable.

Supplementary Text 3. Model description, driver data, configuration, calibration, scenarios, and goodness-of-fit statistics.

Model description

GLM-AED simulates the dominant biogeochemical processes controlling freshwater oxygen and C, N, and P cycling (Farrell et al. 2020, Ward et al. 2020). Water column oxygen dynamics are modeled as a function of atmospheric oxygen exchange, sediment oxygen demand, organic matter mineralization, chemical oxidation (e.g., nitrification), and phytoplankton photosynthesis and respiration. Carbon state variables in GLM-AED include methane (CH_4), dissolved inorganic carbon (DIC), two DOC pools (recalcitrant and labile), particulate organic carbon (POC), and coarse particulate organic matter (CPOM); and C processes include sediment fluxes of CH_4, DOC, DIC, and POC; CH_4 oxidation; mineralization of DOC; decomposition of POC and CPOM; and phytoplankton C fixation, respiration, excretion, and death. Nitrogen state variables in GLM-AED include NH_4^+, NO_3^-, recalcitrant and labile dissolved organic nitrogen (DON), and particulate organic nitrogen (PON); and N processes include sediment fluxes of NH_4^+, NO_3^-, DON, and PON; mineralization of DON; decomposition of PON; nitrification; denitrification; anaerobic ammonium oxidation (anammox); dissimilatory nitrate reduction to ammonium (DNRA); phytoplankton uptake of NH_4^+ and NO_3^-; phytoplankton excretion of DON; and phytoplankton mortality, which affects PON. Phosphorus state variables include DRP, recalcitrant and labile dissolved organic phosphorus (DOP), and particulate organic phosphorus (POP); and P processes include sediment fluxes of DRP, DOP, and POP; mineralization of DOP; decomposition of POP; phytoplankton uptake of DRP; phytoplankton excretion of DOP; and phytoplankton mortality, which affects POP. Total pools - i.e., TOC, TN, and TP - are calculated from summing all of their respective fractions, including phytoplankton C, N, and P pools.

Driver data

GLM-AED simulates the dominant biogeochemical processes controlling freshwater oxygen and carbon, nitrogen, and phosphorus cycling (Hipsey 2014, Farrell et al. 2020, Ward et al. 2020) and requires three driver datasets: meteorological data; inflow stream data (which consists of discharge, water temperature, and chemistry); and outflow water discharge. We developed each of these driver datasets for Falling Creek Reservoir (FCR) for 15 May 2013 to 31 December 2019, as detailed below. All model configuration files and driver data are available in the Environmental Data Initiative repository (Carey et al. 2021d), and the R code (v.3.6.3) to generate the driver files are available in the Zenodo repository (Carey et al. 2021e).

Meteorological driver data: GLM-AED was forced with hourly meteorological data (air temperature, relative humidity, shortwave and longwave radiation, wind speed, and precipitation) from NASA's North American Land Data Assimilation System (NLDAS-2; Xia et al. 2012) for FCR.

Inflow stream driver data: We developed driver datasets of daily discharge and water temperature for the two primary surface streams entering into FCR, Falling Creek and Tunnel Branch (Fig. 2 in main text), from manually-collected data and sensor observations from 2013-2019. The total discharge and temperature of Tunnel Branch, the largest stream that enters into FCR, were measured continuously throughout the study period at a weir with pressure and temperature sensors measuring every 15 minutes (Carey et al. 2021a).

Falling Creek, the smaller stream entering into FCR, was monitored less regularly than the larger inflow and did not have a weir (Supplementary Text 1), so its daily total discharge was summed from separate models that calculated precipitation-driven flow and baseflow. First, we estimated daily precipitation-driven flow for both Falling Creek and Tunnel Branch using a

simple hydrological model based on their delineated watershed areas and NLDAS-2 precipitation and air temperature following Ward et al. (2020); code available in Carey et al. (2021e). Second, we subtracted the modeled daily precipitation-driven flow from total discharge measured at the Tunnel Branch weir to estimate its daily baseflow. Third, we compared baseflow data collected manually in both streams using flowmeters and salt injection on n=19 days without any recent precipitation in 2019 (Carey et al. 2021a), and calculated the mean ratio of baseflow in Falling Creek to Tunnel Branch from those 19 days of data. Fourth, we then multiplied that ratio by the daily baseflow in Tunnel Branch to calculate daily baseflow in Falling Creek. Finally, we summed Falling Creek's daily baseflow and its daily precipitation-driven flow to calculate daily total discharge for that stream.

Water temperature was measured at an upstream littoral site in FCR near where Falling Creek entered the reservoir at approximately the same frequency as the lacustrine monitoring (Supplementary Text 1). This littoral temperature dataset was linearly interpolated and used to calculate Falling Creek's daily inflow temperature (Carey et al. 2021e).

The inflow water chemistry driver data for Tunnel Branch and Falling Creek were determined from manual grab sample observations (Carey et al. 2021f). Both streams are well-mixed, so their dissolved oxygen concentrations were estimated assuming 100% saturation using the rMR package (Moulton 2018). Surface grab samples at Tunnel Branch for NO_3^-, NH_4^+, DRP, DOC, TN, and TP were collected on approximately the same frequency as the reservoir water column chemistry samples (Supplementary Text 1), and linearly interpolated to a daily time step.

GLM-AED requires additional solute driver data for inflows, including dissolved silica (Si); particulate organic fractions of C, N, and P; two dissolved organic fractions of C, N and P

(labile and recalcitrant); dissolved CH_4; and DIC; which were estimated from intermittent grab samples or literature ratios to develop the daily inflow dataset. Specifically, following Wetzel (2001)'s synthesis of the distribution of dissolved, organic, and total fractions of C, N, and P in north temperate lakes similar to FCR, we assumed that: 1) 10% of the DOC, DON, and DOP pools was labile and 90% was recalcitrant; 2) POC concentrations were 10% of DOC concentrations; 3) DON concentrations were five times greater than PON concentrations; and 4) 30% of total organic P is in the DOP fraction. PON concentrations were determined via subtraction, and DIC and dissolved Si concentrations were set at the median of long-term measurements (Munger et al. 2016, Carey et al. 2020). To compensate for not simulating an adsorbed P pool or metal-complexed P pool in the model, we set POP concentrations as ten times the TP concentrations.

Stream water chemistry was measured intermittently at Falling Creek, so its daily solute concentrations were calculated from multiplying Tunnel Branch's daily solute concentrations by ratios of the two stream's solutes measured on n=24 days in 2019 (Carey et al. 2021f).

We represented FCR's hypolimnetic oxygenation system (HOx) by a submerged inflow in the model. The mass of dissolved oxygen in the submerged inflow matched the mass of dissolved oxygen added in the reservoir as part of HOx operations during the field manipulation (Carey et al. 2021d, Carey et al. 2021e), but with a reduced inflow volume (compared to the volume of water pumped through the HOx system) and no other solutes. We simulated the HOx system in this way to recreate how it functions in the reservoir: the HOx system deployed in FCR does not affect water balance or thermal structure because it returns the same volume of water it extracts from 8 m in the hypolimnion for oxygenation onshore back to 8 m without altering its temperature (Gerling et al. 2014). Consequently, because GLM-AED can simulate submerged

inflows but not outflows, we reduced the inflow volume of the submerged stream to avoid altering the model's water budget. We did not add any solutes (other than dissolved oxygen) in this inflow to ensure that any effects of the HOx system on hypolimnetic chemistry were due to in situ reservoir processes, not inflow chemistry dynamics. The water temperature of this submerged inflow was set to observations of water temperature at 8 m, the depth at which the HOx injects the oxygenated water into the hypolimnion (Gerling et al. 2014).

Outflow water balance: The daily outflow discharge was estimated as the sum of the two surface streams' daily inflow discharge, as the reservoir did not exhibit large changes in water level during the 2013-2019 study and was managed to maintain full pond conditions. GLM-AED determines the physical and chemical properties of the outflow using the state of the modeled reservoir.

Model configuration

We simulated two sediment zones in the model, based on the bathymetry of FCR (Gerling et al. 2014), to represent separate epilimnetic and hypolimnetic sediment dynamics. The two sediment zones had different temperature and heat dynamics, as well as different sediment flux rates for oxygen, NH_4^+, NO_3^-, and DRP, following previous work in FCR (Gerling et al. 2016, Krueger et al. 2020, McClure et al. 2020). Phytoplankton were divided into three groups that represented the dominant taxa in FCR: cyanobacteria, diatoms, and green algae (Carey et al. 2021c).

The total model simulation period was 15 May 2013 to 31 December 2019, which was chosen because the weir on the largest stream inflow was deployed on 14 May 2013. GLM-AED was run on an hourly time step throughout the simulation period, which encompassed a wide

range of meteorological conditions, inflow volumes, HOx operation levels, and resulting hypolimnetic oxygen concentrations (Carey et al. 2021d). Initial water column profiles of water temperature and water chemistry were chosen to represent typical conditions observed in the reservoir in May (Carey et al. 2021d).

Model calibration

We divided the total simulation period into calibration (15 May 2013-31 December 2018) and validation (1 January 2019-31 December 2019) periods for model verification. As GLM-AED is a 1-D model, we focused model calibration on the full depth profile at the deepest site at the reservoir, where the long-term monitoring data were collected (Fig. 2 in main text). Earlier studies indicate that oxygen dynamics at the deep site are representative of upstream sites in the reservoir (Gerling et al. 2014, McClure et al. 2018). The monitoring site is immediately adjacent to the reservoir outflow, thereby ensuring that the model accurately captured downstream export of C, N, and P.

We calibrated GLM-AED to observed conditions in a three-step approach, following (Ladwig et al. 2021). First, we conducted a global sensitivity analysis to identify the most important parameters for simulating water temperature, dissolved oxygen, NH_4^+, NO_3^-, DRP, and DOC following Morris (1991). Second, we calibrated the identified sensitive parameters (Table S2) using the covariance matrix adaptation evolution strategy (CMA-ES) for automated numerical optimization to minimize root mean square error (RMSE) between observations and model output (Hansen 2016), using all sampling depths in the water column (0.1, 1.6, 2.8, 3.8, 5.0, 6.2, 8.0, and 9.0 m). Initial parameter values were set at model defaults (Hipsey et al. 2019) and run for 1000 iterations. Third, since we found strong trade-offs in performance for NH_4^+ and

344 NO_3^- automated calibrations, whereby the best parameters for one solute degraded the
345 performance of the other, we manually chose parameter values that exhibited their best combined
346 performance, following (Ladwig et al. 2021). All model parameter values are available in the
347 Environmental Data Initiative repository (Carey et al. 2021d).
348
349 *Goodness-of-fit metrics*
350 We calculated multiple goodness-of-fit metrics to assess the model's performance during
351 the calibration period, the validation period, and the total simulation period for hypolimnetic
352 water temperature, thermocline depth, dissolved oxygen, total and dissolved fractions of C, N,
353 and P water chemistry, and water chemistry ratios. These metrics included Spearman's rho,
354 RMSE, normalized mean absolute error (NMAE), percent bias, and Nash-Sutcliffe Efficiency
355 (NSE), following (Kara et al. 2012, Ward et al. 2020, Ladwig et al. 2021), and are reported in
356 Supplementary Text 4.
357
358 *Model scenarios*
359 We examined the effects of two different oxygen scenarios on the calibrated GLM-AED
360 model: one in which the model was forced with a high level of experimental oxygenation to keep
361 the hypolimnion oxic throughout the summer thermally-stratified period (15 May to 15 Oct) over
362 the 2013-2019 simulation period and one in which zero oxygen was added to the hypolimnion
363 during 2013-2019, so hypolimnetic anoxia quickly set up after the onset of summer thermal
364 stratification each year. The high level of experimental oxygenation in the oxic scenario matched
365 the level of maximum HOx operation in FCR (Carey et al. 2021e). These scenarios were
366 instantiated in the model by modifying the concentration of oxygen in the submerged inflow

oxygen driver file. All other driver data (meteorology, surface stream inflows, outflow) were held constant.

Supplementary Text 4. Comparison of model output and observations.

GLM-AED was able to reproduce observed physical and chemical dynamics when comparing model output and empirical data for 9 m in the hypolimnion (the focus of this study; Table S3), the full water column (Table S4), as well as for the epilimnion only (Fig. S1) during the seven-year REDOX field manipulation. In addition to the state variables reported in the main text, the time series comparison of the modeled and observed focal hypolimnetic (9 m) ratios are presented in Fig. S2.

Supplementary Text 5. Statistical results from paired t-tests comparing anoxic vs. oxic model scenario output.

In the oxic model scenario, oxygen was added into the hypolimnion of Falling Creek Reservoir throughout the thermally-stratified period during each summer of the seven-year study. In the anoxic scenario, no oxygen was added to the hypolimnion, resulting in prolonged hypolimnetic anoxia each summer. We compared the median summer hypolimnetic (9 m) concentrations (Table S5), hypolimnetic molar ratios (Table S6), and reservoir retention of carbon, nitrogen, and phosphorus (Table S7) between the two scenarios with paired t-tests. Daily values were aggregated to summer medians, which were not temporally autocorrelated. We also compared annual rates of sediment burial of particulate organic carbon, nitrogen, and phosphorus between the two scenarios (Table S8).

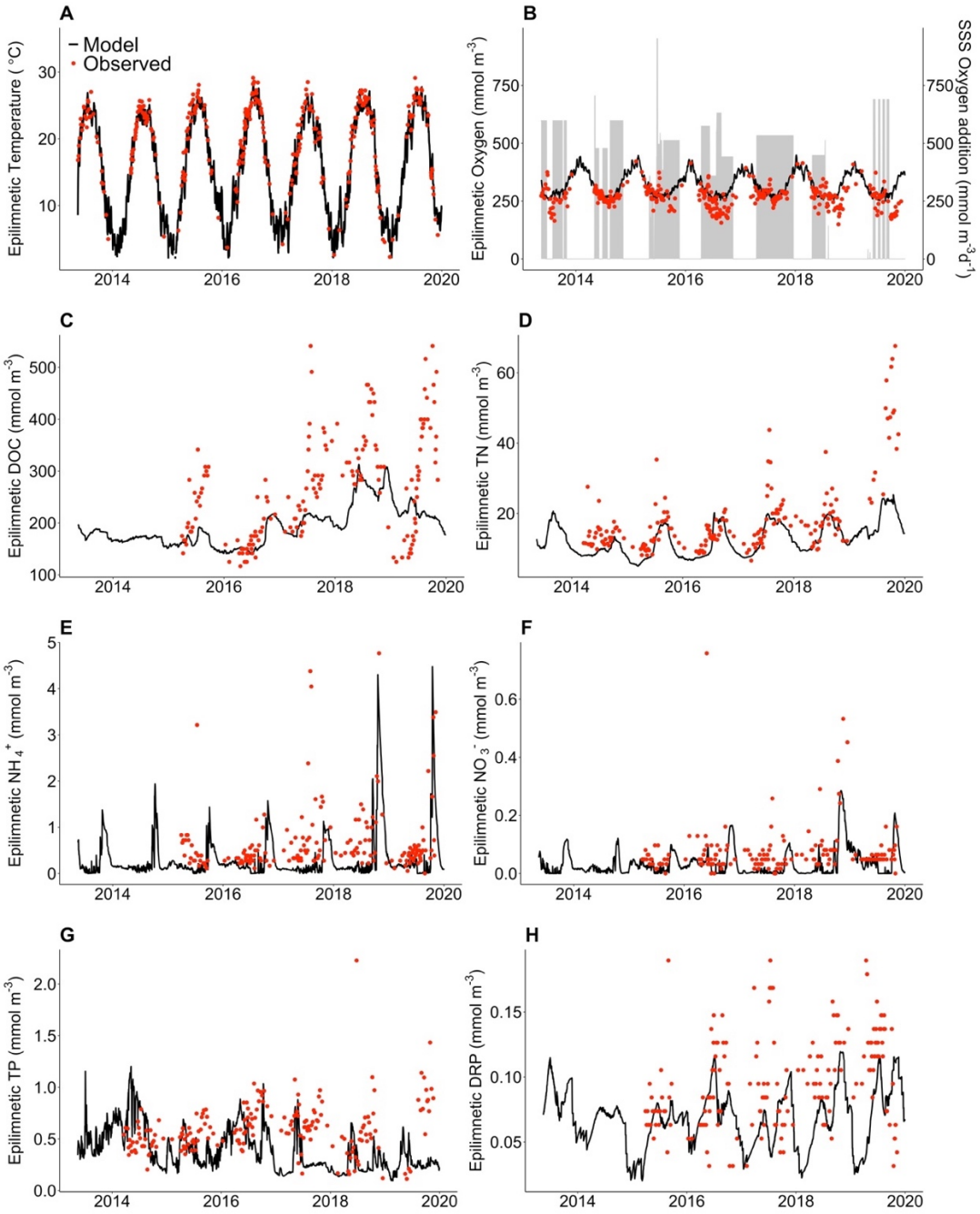

Fig. S1. Modeled vs. observed epilimnetic dynamics in Falling Creek Reservoir. Comparison of modeled (black line) vs. observed (red points) epilimnetic water temperature (A), dissolved oxygen (B), dissolved organic carbon (DOC; C), total nitrogen (TN; D), ammonium (NH_4^+; E), nitrate (NO_3^-; F), total phosphorus (TP; G), and dissolved reactive phosphorus (DRP; H). Epilimnetic water temperature and dissolved oxygen data are from 1 m depth while the water chemistry concentrations are from 1.6 m depth.

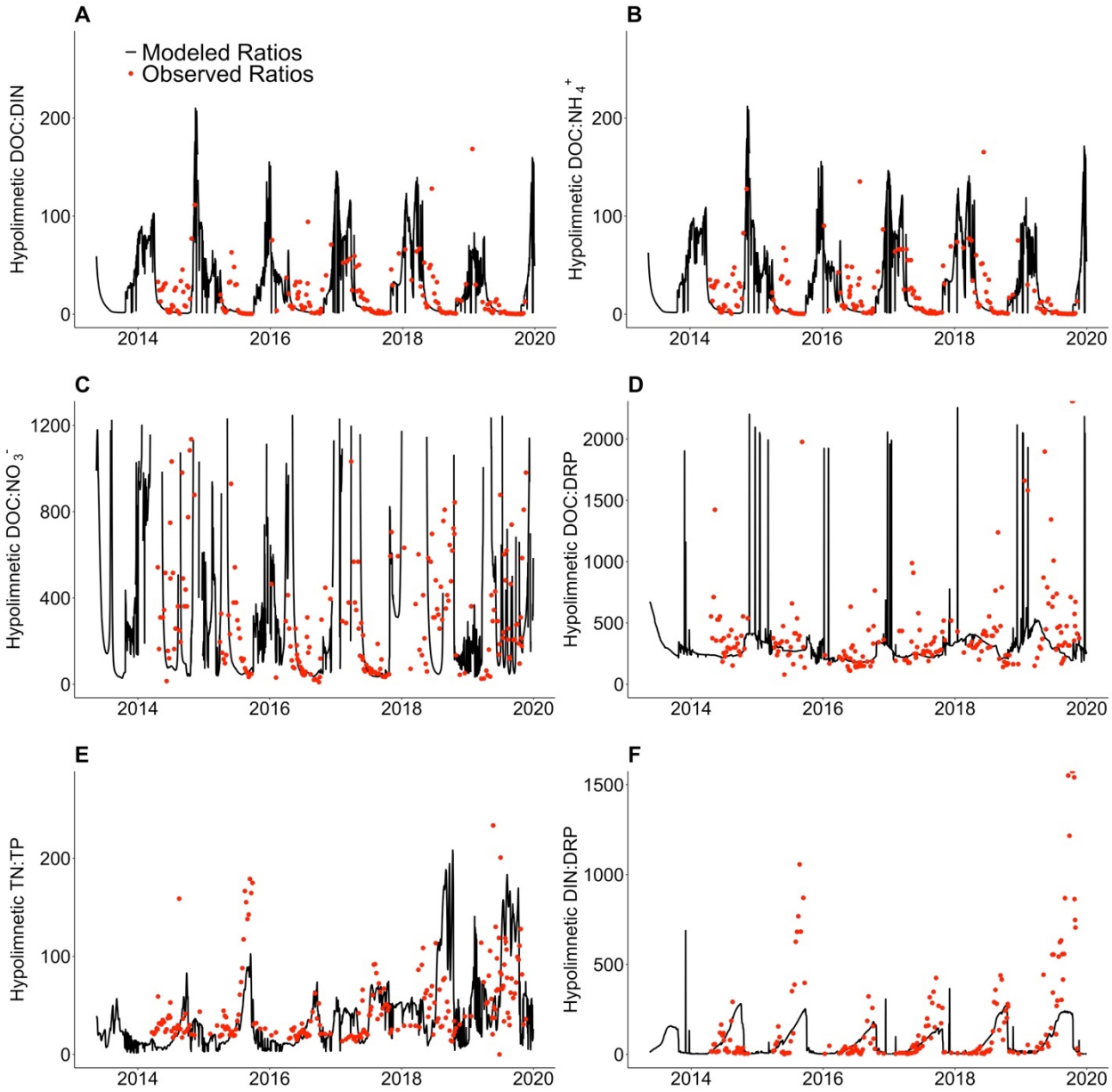

Fig. S2. Modeled vs. observed hypolimnetic stoichiometry in Falling Creek Reservoir. Comparison of modeled (black line) vs. observed (red points) hypolimnetic (9 m) water chemistry molar ratios of dissolved organic carbon to dissolved inorganic nitrogen (DOC:DIN; A), DOC to ammonium (DOC:NH_4^+; B), DOC to nitrate (DOC: NO_3^-; C), DOC to dissolved reactive phosphorus (DOC:DRP; D), total nitrogen to total phosphorus (TN:TP; E), and DIN to DRP (DIN:DRP; F). Note the varying y-axes among panels. Because nitrate concentrations were often below method detection limits, resulting in very large erroneous ratios, only ratios <1250 are presented in panel C.

Table S1. Overview of results of overlap studies between old and new analytical chemistry instruments for each biogeochemical analyte. LOQ denotes limit of quantitation and MDL denotes method detection limit.

Analyte	Old instrument	New instrument	Timing of transition	Number of samples in overlap study	Results of overlap study
Total and dissolved organic carbon	OI Analytical Model 1010 Total Organic Carbon Analyzer (a heated persulfate digestion instrument)	Elementar vario TOC select (a high temperature combustion instrument)	January 2017	302	Only 4% of the observations were below the LOQ. When all samples were included, the Passing-Babcock regression slope was 1.22 (1.17-1.28), the intercept was 0.06 (-0.04 to 0.16), and the Pearson correlation coefficient was 0.967. The slope above 1 suggests that the new method using high temperature combustion may have greater recoveries than the old method using heated persulfate and that this difference may increase with concentration. Plots of residuals over concentration showed no pattern. We chose not to correct concentrations determined before the instrument transition to a modeled equivalence to concentrations determined by the new instrument (e.g., Newell and Morrison 1993) and instead evaluated potential discontinuities over time during that period with particular caution.
Ammonium	Lachat QuikChem 8500 Series 1 Flow Injection Analyzer	Lachat QuikChem 8500 Series 2 Flow Injection Analyzer	Fall 2018	359	We found 24.5% of observations were below the LOQ. When all data were included, the Passing-Babcock regression slope was 1.02 (1.01-1.02), the intercept was -0.48 (-0.80 to 0.06), and the Pearson correlation coefficient was 0.997. While the slope was significantly different from 1, this difference was small. Plots of residuals showed no patterns. When restricted to concentrations above the LOQ, the analysis was largely unchanged. Passing-Babcock regression slope was 1.02 (1.01-1.02), the intercept was -0.54 (-1.00 to 0.25), and the Pearson correlation coefficient was 0.997.
Nitrate	Lachat QuikChem 8500 Series 1 Flow Injection Analyzer	Lachat QuikChem 8500 Series 2 Flow Injection Analyzer	Fall 2018	354	More than half the observations (58.2%) were below the LOQ. When all samples were included the Passing-Babcock regression slope was 1.01 (0.99-1.04), the intercept was -1.05 (-1.26 to -0.84) and the Pearson correlation coefficient was 0.981. While the intercept was significantly different from zero, differences between instruments were

					smaller than the long-term MDL (1.05 and 1.7, respectively). When restricted to concentrations above the LOQ, the analysis was largely unchanged. Passing-Babcock regression slope was 1.02 (1.00-1.06), the intercept was -1.29 (-2.00 to -0.58), and the Pearson correlation coefficient was 0.978.
Total nitrogen	Lachat QuikChem 8500 Series 1 Flow Injection Analyzer	Lachat QuikChem 8500 Series 2 Flow Injection Analyzer	Fall 2018	326	Only one observation was below the LOQ (0.3%). The Passing-Babcock regression slope was 0.98 (0.94-1.02), the intercept was 18.03 (9.01-28.42), and the Pearson correlation coefficient was 0.982. While the intercept was significantly different from zero, the magnitude of the difference between instruments was close to the long-term MDL (18.03 and 14.2 $\mu g\ L^{-1}$ respectively).
Dissolved reactive phosphorus	Lachat QuikChem 8500 Series 1 Flow Injection Analyzer	Lachat QuikChem 8500 Series 2 Flow Injection Analyzer	Fall 2018	356	More than half the observations (64.9%) were below the LOQ. When all samples were included, the Passing-Babcock regression slope was 0.76 (0.71-0.80), the intercept was 0.27 (-0.22 to 0.63), and the Pearson correlation coefficient was 0.958. The method comparison plot shows a flattening of the slope at concentration below the LOQ. Plots of residuals suggest a U-shape with an increase at the highest and lowest concentrations. When restricted to concentrations above the LOQ, Passing-Babcock regression slope was 0.99 (0.92-1.06), the intercept was -3.39 (-4.79 to -2.12), and the Pearson correlation coefficient was 0.966. Plots of residuals over concentration were randomly distributed around 0. While the intercept was significantly different from zero, the magnitude of the difference between instruments was close to the long-term MDL (3.39 and 2.5, respectively). For this analyte in particular, caution is warranted when interpreting potential differences in concentration below the LOQ.
Total phosphorus	Lachat QuikChem 8500 Series 1 Flow Injection Analyzer	Lachat QuikChem 8500 Series 2 Flow Injection Analyzer	Fall 2018	336	More than half the observations were below the LOQ (56.0%). The Passing-Babcock regression slope was 0.95 (0.92-0.98), the intercept was 3.24 (2.78-3.72), and the Pearson correlation coefficient was 0.954. When restricted to concentrations above the LOQ, Passing-Babcock regression slope was 1.05 (1.01-1.09), the intercept was 0.78 (-0.39 to 1.82), and the Pearson correlation

					coefficient was 0.960. While the slope was significantly different from 1, this difference was small. Plots of residuals showed no patterns. For this analyte in particular, caution is warranted when interpreting potential differences in concentration below the LOQ.

409

Table S2. GLM-AED parameters that were identified as highly sensitive for the focal state variables in the Falling Creek Reservoir model. The focal state variables were water temperature, dissolved oxygen, dissolved organic carbon (DOC), ammonium (NH_4^+), nitrate (NO_3^-), and dissolved reactive phosphorus (DRP).

State variables	**Calibrated parameters**
Temperature	Coef_mix_hyp, sw_factor, lw_factor, ch, sed_temp_mean, sed_temp_amplitude, sed_temp_peak_doy
Dissolved oxygen	Fsed_oxy, Ksed_oxy
DOC	Kdom_minerl, Kpom_hydrol
NH_4^+	Fsed_amm, Ksed_amm, Rnitrif, Knitrif, theta_nitrif, Kdnra_oxy, Kanmx_amm
NO_3^-	Rnitrif
DRP	Fsed_frp, Ksed_frp

Table S3. Goodness-of-fit (GOF) metrics for comparing observations and modeled GLM-AED output for Falling Creek Reservoir, VA, USA in the hypolimnion (9 m). GOF metrics include root mean square error (RMSE), percent bias (%PBIAS), Nash-Sutcliffe (NSE), Pearson's correlation coefficient (Pearson's r), and normalized mean absolute error (NMAE); *n* is the number of observed measurements. Each GOF metric was calculated comparing model outputs and observational data for the time period of interest (Full simulation, 2013-2019; Calibration, 2013-2018; and Validation, 2018-2019). Evaluated parameters include temperature (Temp, ^{o}C), oxygen (mmol m^{-3}), ammonium (NH_4^+, mmol m^{-3}), nitrate (NO_3^-, mmol m^{-3}), dissolved reactive phosphorus (DRP, mmol m^{-3}), dissolved organic carbon (DOC, mmol m^{-3}), total nitrogen (TN, mmol m^{-3}), and total phosphorus (TP, mmol m^{-3}). We note that the model fits for TP and DRP, while in the magnitude of the observations, were worse than for the other solutes. This is likely due to measurement uncertainty, rather than model misspecification, since most of the TP and DRP observations were below the limit of quantitation in laboratory analysis (0.15 and 0.08 mmol m^{-3}, respectively).

Time period	Parameter	Temp	Oxygen	NH_4^+	NO_3^-	DRP	DOC	TN	TP
Full simulation	*n*	323	331	201	201	200	201	229	230
	RMSE	1.32	97.5	14.6	0.24	0.06	63.2	18.9	0.65
	PBIAS%	2.8	9.0	-3.1	29.1	30.2	-3.4	-26.4	-3.5
	NSE	0.75	0.17	0.32	-0.43	-1.21	0.24	0.33	-0.39
	Pearson's r	0.89	0.69	0.64	0.30	0.01	0.53	0.70	0.09
	NMAE	0.10	0.39	0.73	1.05	0.59	0.21	0.42	0.64
Calibration	*n*	277	285	162	162	161	162	180	181
	RMSE	1.33	100.7	13.8	0.22	0.05	51.0	16.6	0.6
	PBIAS%	1.6	7.1	14.4	24.5	14.4	-7.3	-25.0	3.4
	NSE	0.76	0.01	0.06	-0.18	-0.37	0.44	0.13	-0.35
	Pearson's r	0.89	0.64	0.60	0.38	0.05	0.77	0.65	0.10
	NMAE	0.10	0.37	0.93	0.87	0.41	0.17	0.43	0.61
Validation	*n*	46	46	39	39	39	39	49	49
	RMSE	1.26	74.2	17.2	0.3	0.09	98.9	25.8	0.60
	PBIAS%	10.1	32.7	-28.3	56.0	130.3	12.9	-29.1	-28.6
	NSE	0.69	0.39	0.47	-2.45	-7.91	-0.25	0.29	-0.61
	Pearson's r	0.95	0.80	0.77	0.00	0.04	-0.39	0.62	0.06
	NMAE	0.10	0.53	0.44	1.72	1.46	0.39	0.39	0.75

Table S4. Goodness-of-fit (GOF) metrics for comparing observations and modeled GLM-AED output for Falling Creek Reservoir, VA, USA in the entire water column (aggregated across 0.1, 1.6, 2.8, 3.8, 5.0, 6.2, 8.0, and 9.0 m observations). GOF metrics include root mean square error (RMSE), percent bias (%PBIAS), Nash-Sutcliffe (NSE), Pearson's correlation coefficient (Pearson's r), and normalized mean absolute error (NMAE); *n* is the number of observed measurements. Each GOF metric was calculated comparing model outputs and observational data for the time period of interest (Full time period, 2013-2019; Calibration, 2013-2018; and Validation, 2018-2019). Evaluated parameters include temperature (Temp, ^{o}C), thermocline depth (TD, m), oxygen (mmol m^{-3}), ammonium (NH_4^+, mmol m^{-3}), nitrate (NO_3^-, mmol m^{-3}), dissolved reactive phosphorus (DRP, mmol m^{-3}), dissolved organic carbon (DOC, mmol m^{-3}), total nitrogen (TN, mmol m^{-3}), and total phosphorus (TP, mmol m^{-3}). Thermocline depth was calculated using LakeAnalyzer (Read et al. 2011). We note that the model fits for TP and DRP, while in the magnitude of the observations, were worse than for the other solutes. This is likely due to measurement uncertainty, rather than model misspecification, since most of the TP and DRP observations were below the limit of quantitation in laboratory analysis (0.15 and 0.08 mmol m^{-3}, respectively).

Time period	**Parameter**	**Temp**	**TD**	**Oxygen**	**NH_4^+**	**NO_3^-**	**DRP**	**DOC**	**TN**	**TP**
Full simulation	*n*	3639	356	3726	1277	1273	1271	1277	1518	1724
	RMSE	1.89	1.5	81.2	8.34	0.16	0.05	81.9	12.1	0.54
	PBIAS%	1.7	3.6	5.5	18	7.7	11.8	-12.5	-21.3	-11.6
	NSE	0.89	0.01	0.32	0.4	-0.34	-0.93	0.12	0.36	-0.78
	Pearson's r	0.94	0.32	0.63	0.56	0.22	0.03	0.53	0.73	0.08
	NMAE	0.10	0.30	0.27	0.82	0.94	0.52	0.25	0.36	0.58
Calibration	*n*	3164	309	3251	1018	1014	1012	1018	1250	1456
	RMSE	1.90	1.5	80.6	8.07	0.15	0.04	68.9	9.9	0.53
	PBIAS%	0.7	1.6	4.8	42.7	7.0	0.90	-14.3	-17.7	-8.2
	NSE	0.89	0.02	0.26	-0.07	-0.16	-0.45	0.24	0.11	-0.9
	Pearson's r	0.94	0.31	0.61	0.49	0.27	0.06	0.75	0.69	0.05
	NMAE	0.10	0.31	0.26	1.08	0.91	0.37	0.20	0.34	0.57
Validation	*n*	475	47	475	259	259	259	259	268	268
	RMSE	1.87	1.1	84.7	9.27	0.18	0.07	119.0	19.5	0.55
	PBIAS%	8.7	19.4	11.8	-13.7	10.4	68.3	-6.1	-29.6	-32.1
	NSE	0.89	-0.42	0.46	0.70	-1.33	-2.97	-0.15	0.23	-0.38
	Pearson's r	0.97	0.46	0.73	0.79	-0.02	0.09	-0.53	0.59	0.06
	NMAE	0.11	0.23	0.38	0.46	1.25	1.02	0.41	0.39	0.70

Table S5. Paired t-test results comparing median summer stratified period (July 15-October 1) hypolimnetic (9 m) concentrations in anoxic vs. oxic model scenarios for Falling Creek Reservoir during the seven years of the study. The variables compared were total organic carbon (TOC), dissolved organic carbon (DOC), total nitrogen (TN), dissolved inorganic nitrogen (DIN), ammonium (NH_4^+), nitrate (NO_3^-), total phosphorus (TP), and dissolved reactive phosphorus (DRP). df denotes degrees of freedom.

Variable	**t-value**	**df**	**p-value**
TOC	14.72	6	p<0.0001
DOC	15.59	6	p<0.0001
TN	18.64	6	p<0.0001
DIN	18.5	6	p<0.0001
NH_4^+	-9.31	6	p<0.0001
NO_3^-	9.39	6	p<0.0001
TP	16.61	6	p<0.0001
DRP	14.72	6	p<0.0001

Table S6. Paired t-test results comparing median summer stratified period (July 15 - October 1) total and dissolved molar ratios of hypolimnetic (9 m) carbon, nitrogen, and phosphorus concentrations for Falling Creek Reservoir during the seven years of the study. The variables compared included the ratios of total organic carbon to total nitrogen (TOC:TN), TOC to total phosphorus (TOC:TP), dissolved organic carbon to dissolved inorganic nitrogen (DOC:DIN), DOC to ammonium (DOC:NH_4^+), DOC to nitrate (DOC:NO_3^-), DOC to dissolved reactive phosphorus (DOC:DRP), TN:TP, and DIN:DRP. df denotes degrees of freedom. Because NO_3^- concentrations functionally went to zero during anoxia, DOC:NO_3^- could not be calculated and hence there are no t-test results for this ratio.

Variable	**t-value**	**df**	**p-value**
TOC:TN	-11.02	6	p<0.0001
TOC:TP	-2.03	6	0.09
DOC:DIN	-8.14	6	0.0002
DOC:NH_4^+	-7.78	6	0.0002
DOC:NO_3^-	.	.	.
DOC:DRP	-7.11	6	0.0004
TN:TP	5.77	6	0.001
DIN:DRP	10.76	6	p<0.0001

Table S7. Paired t-test results comparing median summer stratified period (July 15-October 1) retention of carbon, nitrogen, and phosphorus entering into Falling Creek Reservoir in anoxic vs. oxic model scenarios during the seven years of the study. The variables compared were total organic carbon (TOC), dissolved organic carbon (DOC), total nitrogen (TN), dissolved inorganic nitrogen (DIN), ammonium (NH_4^+), nitrate (NO_3^-), total phosphorus (TP), and dissolved reactive phosphorus (DRP). df denotes degrees of freedom.

Variable	**t-value**	**df**	**p-value**
TOC	11.56	6	p<0.0001
DOC	11.83	6	p<0.0001
TN	21.19	6	p<0.0001
DIN	8.74	6	0.0001
NH_4^+	6.5	6	0.0006
NO_3^-	-4.78	6	0.003
TP	5.95	6	0.001
DRP	8.99	6	0.0001

Table S8. Paired t-test results comparing annual sediment burial rates of particulate organic carbon (POC), particulate organic nitrogen (PON), and particulate organic phosphorus (POP) in Falling Creek Reservoir in anoxic vs. oxic model scenarios of the seven years of the study. df denotes degrees of freedom.

Variable	**t-value**	**df**	**p-value**
POC	-1.98	5	0.10
PON	-3.46	5	0.02
POP	-1.06	5	0.34

References

APHA. 2017a. Method 4500-NH3 H. Nitrogen (ammonia) flow injection analysis. Standard Methods for the Examination of Water and Wastewater, 23rd Ed. American Public Health Association, American Water Works Association, Washington, DC.

APHA. 2017b. Method 4500-NO3 I. Nitrogen (nitrate) cadmium reduction flow injection method. Standard Methods for the Examination of Water and Wastewater, 23rd Ed. American Public Health Association, American Water Works Association, Washington, DC.

APHA. 2017c. Method 4500-P G. Flow injection analysis for orthophosphate. Standard Methods for the Examination of Water and Wastewater, 23rd Ed. American Public Health Association, American Water Works Association, Washington, DC.

APHA. 2017d. Method 5310B. Total organic carbon (TOC): high-temperature combustion method. Standard Methods for the Examination of Water and Wastewater, 23rd Ed. American Public Health Association, American Water Works Association, Washington, DC.

APHA. 2017e. Method 5310C. Total organic carbon (TOC): persulfate-ultraviolet or heated-persulfate oxidation method. Standard Methods for the Examination of Water and Wastewater, 23rd Ed. American Public Health Association, American Water Works Association, Washington, DC.

Carey, C. C., J. P. Doubek, R. P. McClure, and P. C. Hanson. 2018. Oxygen dynamics control the burial of organic carbon in a eutrophic reservoir. Limnology and Oceanography Letters **3**:293-301.

Carey, C. C., J. P. Doubek, J. H. Wynne, and B. R. Niederlehner. 2020. Dissolved silica time series for Beaverdam Reservoir, Carvins Cove Reservoir, Claytor Lake, Falling Creek Reservoir, Gatewood Reservoir, Smith Mountain Lake, and Spring Hollow Reservoir in southwestern Virginia, USA during 2014 ver 1. Environmental Data Initiative repository. https://doi.org/10.6073/pasta/353aa34bedfd68800c12275633811341

Carey, C. C., A. G. Hounshell, M. E. Lofton, B. Birgand, B. J. Bookout, R. S. Corrigan, A. B. Gerling, R. P. McClure, and W. M. Woelmer. 2021a. Discharge time series for the primary inflow tributary entering Falling Creek Reservoir, Vinton, Virginia, USA 2013-2021 ver 7. Environmental Data Initiative repository. https://doi.org/10.6073/pasta/8d22a432aac5560b0f45aa1b21ae4746

Carey, C. C., A. S. Lewis, R. P. McClure, A. B. Gerling, S. Chen, A. Das, J. P. Doubek, D. W. Howard, M. E. Lofton, K. D. Hamre, and H. L. Wander. 2021b. Time series of high-frequency profiles of depth, temperature, dissolved oxygen, conductivity, specific conductivity, chlorophyll a, turbidity, pH, oxidation-reduction potential, photosynthetic active radiation, and descent rate for Beaverdam Reservoir, Carvins Cove Reservoir, Falling Creek Reservoir, Gatewood Reservoir, and Spring Hollow Reservoir in Southwestern Virginia, USA 2013-2020 ver 11. Environmental Data Initiative repository. https://doi.org/10.6073/pasta/5448f9d415fd09e0090a46b9d4020ccc

Carey, C. C., M. E. Lofton, W. M. Woelmer, K. D. Hamre, A. Breef-Pilz, J. P. Doubek, and R. P. McClure. 2021c. Carey, C.C., M.E. Lofton, W.M. Woelmer, K.D. Hamre, A. Breef-Pilz, J.P. Doubek, and R.P. McClure. 2021. Time-series of high-frequency profiles of fluorescence-based phytoplankton spectral groups in Beaverdam Reservoir, Carvins Cove Reservoir, Falling Creek Reservoir, Gatewood Reservoir, and Spring Hollow Reservoir

in southwestern Virginia, USA 2014-2020 ver 5. Environmental Data Initiative repository. https://doi.org/10.6073/pasta/54d4bd2fee1e52e36e2b0f230912d2da

Carey, C. C., R. Q. Thomas, and P. C. Hanson. 2021d. General Lake Model-Aquatic EcoDynamics model parameter set for Falling Creek Reservoir, Vinton, Virginia, USA 2013-2019, ver 2. Environmental Data Initiative repository, https://portal-s.edirepository.org/nis/mapbrowse?packageid=edi.471.2.

Carey, C. C., R. Q. Thomas, R. P. McClure, A. G. Hounshell, W. M. Woelmer, H. L. Wander, and A. S. L. Lewis. 2021e. CareyLabVT/FCR-GLM: FCR GLM-AED model, data, and code for Carey et al. manuscript (v1.0). Zenodo, https://doi.org/10.5281/zenodo.5528865.

Carey, C. C., H. L. Wander, W. M. Woelmer, M. E. Lofton, A. Breef-Pilz, J. P. Doubek, A. B. Gerling, A. G. Hounshell, R. P. McClure, and B. R. Niederlehner. 2021f. Water chemistry time series for Beaverdam Reservoir, Carvins Cove Reservoir, Falling Creek Reservoir, Gatewood Reservoir, and Spring Hollow Reservoir in southwestern Virginia, USA 2013-2020 ver 8. Environmental Data Initiative repository. https://doi.org/10.6073/pasta/8d83ef7ec202eca9192e3da6dd34a4e0

Carey, C. C., W. M. Woelmer, J. T. Maze, and A. G. Hounshell. 2019. Manually-collected discharge data for multiple inflow tributaries entering Falling Creek Reservoir and Beaverdam Reservoir, Vinton, Virginia, USA in 2019 ver 4. Environmental Data Initiative repository. https://doi.org/10.6073/pasta/4d8e7b7bedbc6507b307ba2d5f2cf9a2

Carey, C. C., J. H. Wynne, H. L. Wander, R. P. McClure, K. J. Farrell, A. Breef-Pilz, J. P. Doubek, A. B. Gerling, K. D. Hamre, A. G. Hounshell, A. S. Lewis, M. E. Lofton, and W. M. Woelmer. 2021g. Secchi depth data and discrete depth profiles of photosynthetically active radiation, temperature, dissolved oxygen, and pH for

Beaverdam Reservoir, Carvins Cove Reservoir, Falling Creek Reservoir, Gatewood Reservoir, and Spring Hollow Reservoir in southwestern Virginia, USA 2013-2020, ver 8. Environmental Data Initiative repository. https://doi.org/10.6073/pasta/3e9f27971e353c8a80840b5e99a67d0c

Currie, L. A. 1968. Limits for qualitative detection and quantitative determination. Application to radiochemistry. Analytical Chemistry **40**:586-593.

Doyle, A., M. N. Weintraub, and J. P. Schimel. 2004. Persulfate digestion and simultaneous colorimetric analysis of carbon and nitrogen in soil extracts. Soil Science Society of America Journal **68**:669-676.

Egan, L. 2013. Determination of Total Nitrogen in Manual Persulfate Digests. Low Flow Method. QuikChem Method 10-107-04-4-C. Lachat Instruments Loveland, CO.

Farrell, K. J., N. K. Ward, A. I. Krinos, P. C. Hanson, V. Daneshmand, R. J. Figueiredo, and C. C. Carey. 2020. Ecosystem-scale nutrient cycling responses to increasing air temperatures vary with lake trophic state. Ecological Modelling **430**:109134.

Gerling, A., R. Browne, P. Gantzer, M. Mobley, J. Little, and C. Carey. 2014. First report of the successful operation of a side stream supersaturation hypolimnetic oxygenation system in a eutrophic, shallow reservoir. Water Research **67**:129-143.

Gerling, A. B., Z. W. Munger, J. P. Doubek, K. D. Hamre, P. A. Gantzer, J. C. Little, and C. C. Carey. 2016. Whole-catchment manipulations of internal and external loading reveal the sensitivity of a century-old reservoir to hypoxia. Ecosystems **19**:555-571.

Gordon, N. D., T.A. McMahon, B.L. Finlayson. 2004. Stream Hydrology: an Introduction for Ecologists, 2nd edition. John Wiley & Sons, Inc., New York.

Grasshoff, K., and H. Johannsen. 1972. A new sensitive and direct method for the automatic determination of ammonia in sea water. ICES Journal of Marine Science **34**:516-521.

Hansen, N. 2016. The CMA evolution strategy: A tutorial. ArXiv **160400772**.

Hipsey, M. R., L. C. Bruce, C. Boon, B. Busch, C. C. Carey, D. P. Hamilton, P. C. Hanson, J. S. Read, E. de Sousa, M. Weber, and L. A. Winslow. 2019. A General Lake Model (GLM 3.0) for linking with high-frequency sensor data from the Global Lake Ecological Observatory Network (GLEON). Geoscience Model Development **12**:473-523.

Hipsey, M. R., Bruce, L.C., Hamilton, D.P. 2014. GLM - General Lake Model: Model overview and user information. The University of Western Australia, Perth, Australia.

Huang, X.-L., and J.-Z. Zhang. 2009. Neutral persulfate digestion at sub-boiling temperature in an oven for total dissolved phosphorus determination in natural waters. Talanta **78**:1129-1135.

IUPAC. 1997. International Union of Pure and Applied Chemistry 1997 IUPAC Compendium of Analytical Nomenclature, Definitive Rules, 3rd edition. Blackwell Science, London.

Kara, E. L., P. Hanson, D. Hamilton, M. R. Hipsey, K. D. McMahon, J. S. Read, L. Winslow, J. Dedrick, K. Rose, C. C. Carey, S. Bertilsson, D. da Motta Marques, L. Beversdorf, T. Miller, C. Wu, Y.-F. Hsieh, E. Gaiser, and T. Kratz. 2012. Time-scale dependence in numerical simulations: Assessment of physical, chemical, and biological predictions in a stratified lake at temporal scales of hours to months. Environmental Modelling & Software **35**:104-121.

Krueger, K. M., C. E. Vavrus, M. E. Lofton, R. P. McClure, P. Gantzer, C. C. Carey, and M. E. Schreiber. 2020. Iron and manganese fluxes across the sediment-water interface in a drinking water reservoir. Water Research **182**:116003.

Lachat. 2007a. Determination of ammonia by flow injection analysis. Low flow method. QuikChem Method 10-107-06-1-J. Lachat Instruments Loveland, CO.

Lachat. 2007b. Determination of orthophosphate by flow injection analysis. Low flow method. QuikChem Method 10-115-10-1-Q. Lachat Instruments Loveland, CO.

Ladwig, R., P. C. Hanson, H. A. Dugan, C. C. Carey, Y. Zhang, L. Shu, C. J. Duffy, and K. M. Cobourn. 2021. Lake thermal structure drives interannual variability in summer anoxia dynamics in a eutrophic lake over 37 years. Hydrology and Earth System Sciences **25**:1009-1032.

Lynch, D. 2007. Determination of nitrate/nitrite by flow injection analysis. Low flow method. QuikChem Method 10-107-04-1-L. Lachat Instruments, Loveland, CO.

Manuilova, E., and A. Schuetzenmeister. 2014. mcr: Method Comparison. Regression. R package version 1.2.1.

McClure, R., K. Hamre, B. Niederlehner, Z. Munger, S. Chen, M. Lofton, M. Schreiber, and C. Carey. 2018. Metalimnetic oxygen minima alter the vertical profiles of carbon dioxide and methane in a managed freshwater reservoir. The Science of the Total Environment **636**:610-620.

McClure, R. P., M. E. Lofton, S. Chen, K. M. Krueger, J. C. Little, and C. C. Carey. 2020. The magnitude and drivers of methane ebullition and diffusion vary on a longitudinal gradient in a small freshwater reservoir. Journal of Geophysical Research: Biogeosciences **125**:e2019JG005205.

McDonald, C. P., E. G. Stets, R. G. Striegl, and D. Butman. 2013. Inorganic carbon loading as a primary driver of dissolved carbon dioxide concentrations in the lakes and reservoirs of the contiguous United States. Global Biogeochemical Cycles **27**:285-295.

613 Mendonça, R., R. A. Müller, D. Clow, C. Verpoorter, P. Raymond, L. J. Tranvik, and S. Sobek.
614 2017. Organic carbon burial in global lakes and reservoirs. Nature Communications
615 **8**:1694.
616 Morris, M. D. 1991. Factorial sampling plans for preliminary computational experiments.
617 Technometrics **33**:161-174.
618 Moulton, T. L. 2018. rMR: Calculating Metabolic Rates and Critical Tensions. R package
619 version 1.1.0.
620 Munger, Z., C. Carey, A. Gerling, K. Hamre, J. Doubek, S. Klepatzki, R. McClure, and M.
621 Schreiber. 2016. Effectiveness of hypolimnetic oxygenation for preventing accumulation
622 of Fe and Mn in a drinking water reservoir. Water Research **106**:1-14.
623 Newell, A. D., and M. L. Morrison. 1993. Use of overlap studies to evaluate method changes in
624 water chemistry protocols. Water, Air, and Soil Pollution **67**:433-456.
625 Passing, H., and Bablok. 1983. A new biometrical procedure for testing the equality of
626 measurements from two different analytical methods. Application of linear regression
627 procedures for method comparison studies in clinical chemistry, Part I. Journal of
628 Clinical Chemistry and Clinical Biochemistry **21**:709-720.
629 Patton, C. J., and J. R. Kryskalla. 2003. Methods of analysis by the U.S. Geological Survey
630 National Water Quality Laboratory—Evaluation of alkaline persulfate digestion as an
631 alternative to Kjeldahl digestion for determination of total and dissolved nitrogen and
632 phosphorus in water. USGS Water-Resources Investigations Report 2003-4174.
633 Ranke, J. 2018. chemCal: Calibration functions for analytical chemistry. R package version
634 0.2.1.

635 Read, J. S., D. P. Hamilton, I. D. Jones, K. Muraoka, L. A. Winslow, R. Kroiss, C. H. Wu, and
636 E. Gaiser. 2011. Derivation of lake mixing and stratification indices from high-resolution
637 lake buoy data. Environmental Modelling & Software **26**:1325-1336.
638 Team, R. C. 2020. R: A language and environment for statistical computing. Version 3.6.3. R
639 Foundation for Statistical Computing, Vienna, Austria.
640 USEPA. 1997. Appendix B to Part 136 - Definition and Procedure for the Determination of the
641 Method Detection Limit - Revision 1.11. U.S. Environmental Protection Agency.
642 Ward, N. K., B. G. Steele, K. C. Weathers, K. L. Cottingham, H. A. Ewing, P. C. Hanson, and C.
643 C. Carey. 2020. Differential responses of maximum versus median chlorophyll-a to air
644 temperature and nutrient loads in an oligotrophic lake over 31 years. Water Resources
645 Research **56**:e2020WR027296.
646 Wetzel, R. G. 2001. Limnology: Lake and River Ecosystems. 3rd edition. Academic Press, New
647 York.
648 Wetzel, R. G., and G. E. Likens. 2000. Exercise 7. Inorganic nutrients: Nitrogen, phosphorus,
649 and other nutrients. Pages 85-111 *in* Limnological Analyses. 3rd ed. Springer, New York.
650 Xia, Y., K. Mitchell, M. Ek, J. Sheffield, B. Cosgrove, E. Wood, L. Luo, C. Alonge, H. Wei, J.
651 Meng, B. Livneh, D. Lettenmaier, V. Koren, Q. Duan, K. Mo, Y. Fan, and D. Mocko.
652 2012. Continental-scale water and energy flux analysis and validation for the North
653 American Land Data Assimilation System project phase 2 (NLDAS-2): 1.
654 Intercomparison and application of model products. Journal of Geophysical Research:
655 Atmospheres **117**:D03109.
656 Zhang, J. Z., P. B. Ortner, C. J. Fischer, and L. D. Moore. 1997. Method 349.0 Determination of
657 ammonia in estuarine and coastal waters by gas segmented flow continous flow

colorimetric analysis. Methods for determination of chemical substances in marine and estuarine environmental matrices, 2nd ed. Environmental Protection Agency, Washington, D.C.